Journal Pre-proof

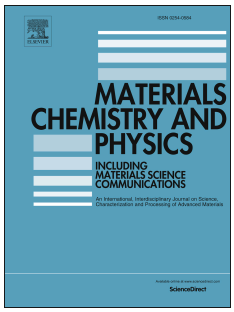

Effect of laser induced remelting on the scratch behavior of spark plasma sintered nickel aluminide alloy

Gülşah Aktaş Çelik, Fatih Aksu, F. Betül Yılmaz Güler, Satılmış Ürgün, Sinan Fidan, M. Özgür Bora, Yunus Erbay, Ş. Hakan Atapek

PII: S0254-0584(25)00838-7

DOI: https://doi.org/10.1016/j.matchemphys.2025.131192

Reference: MAC 131192

To appear in: *Materials Chemistry and Physics*

Received Date: 27 March 2025

Revised Date: 16 May 2025

Accepted Date: 22 June 2025

Please cite this article as: G.A. Çelik, F. Aksu, F.B. Yılmaz Güler, S. Ürgün, S. Fidan, M.Ö. Bora, Y. Erbay, Ş.H. Atapek, Effect of laser induced remelting on the scratch behavior of spark plasma sintered nickel aluminide alloy, *Materials Chemistry and Physics*, https://doi.org/10.1016/j.matchemphys.2025.131192.

This is a PDF file of an article that has undergone enhancements after acceptance, such as the addition of a cover page and metadata, and formatting for readability, but it is not yet the definitive version of record. This version will undergo additional copyediting, typesetting and review before it is published in its final form, but we are providing this version to give early visibility of the article. Please note that, during the production process, errors may be discovered which could affect the content, and all legal disclaimers that apply to the journal pertain.

© 2025 Published by Elsevier B.V.

Journal Pre-proof

Effect of laser induced remelting on the scratch behavior of spark plasma sintered nickel aluminide alloy

Gülşah Aktaş Çelik[1], Fatih Aksu[1], F. Betül Yılmaz Güler[1], Satılmış Ürgün[2], Sinan Fidan[3], M. Özgür Bora[3], Yunus Erbay[4], Ş. Hakan Atapek[1,]*

[1]Kocaeli University, Faculty of Engineering, Department of Metallurgical and Materials Engineering, Laboratory of High Temperature Materials, Kocaeli, Türkiye

[2]Kocaeli University, Faculty of Aeronautics and Astronautics, Department of Aviation Electrics and Electronics, Kocaeli, Türkiye

[3]Kocaeli University, Faculty of Aeronautics and Astronautics, Department of Airframe & Powerplant Maintenance, Kocaeli, Türkiye

[4]Hartek Diamond Cutting Tools Co., Istanbul, Türkiye.

Nickel aluminide (NiAl) alloys produced by spark plasma sintering (SPS) present high potential for high-temperature application due to their superior mechanical and oxidation properties. However, their intrinsic brittleness and susceptibility to wear require treatment of their surface. In this work, the impact of laser-induced remelting (LIR) on the scratch behavior of SPS-processed NiAl alloys under different conditions of processing is studied. The parameters of laser power (30, 50, and 75 W), scanning speed (1000 and 2000 mm/s), and processing atmospheres (air and argon) were modified in sequence to investigate microstructure development and mechanical performance. Thermodynamic simulation of phase stability and solidification paths using Thermo-Calc software determined equilibrium phase stability and solidification paths. Scheil simulations proved Al depletion in remelt zones, which modified phase balance of NiAl and Ni_3Al. The phase transition was proved using X-ray Diffractometer (XRD), while microstructure refinement and redistributions in elements were identified using scanning electron microscope (SEM) and energy-dispersive X-ray spectrometer (EDS). The scratch tests indicated that LIR significantly enhanced scratch resistance, which reduced wear depth by up to 40% at loads of 5N and 15N. The smooth topography of surfaces upon remelting was proved using 3D profilometry. The findings indicate high potential of using LIR to generate designed NiAl surface properties for application in aerospace and high-performance engineering.

Keywords: Nickel aluminide, SPS, laser induced remelting, wear.

* *Corresponding author*

Prof. Dr. Ş. Hakan Atapek, Kocaeli University, Faculty of Engineering, Department of Metallurgical and Materials Engineering, Laboratory of High Temperature Materials, Kocaeli, Türkiye

E-mail : hatapek@kocaeli.edu.tr Tel : +90 262 303 30 76 Fax : +90 262 303 30 03

Journal Pre-proof

1. Introduction

For high-temperature applications, intermetallic nickel aluminide NiAl has been subjected to much research interest as possible alternatives to nickel-based superalloys. The extraordinary properties of NiAl and its high-temperature applications result from strong bonding between aluminum and nickel retained at elevated temperatures. By this particular quality, it gives NiAl a good mechanical strength, stability, and resistance to oxidation, hence enabling them to be used alongside conventional superalloys. As a result, NiAl intermetallics are being thoroughly researched for cutting-edge energy, automotive, and aerospace applications where improved performance in extremely hot environments is essential [1]. Ni_3Al, NiAl, and $NiAl_3$ are all members of the nickel aluminide group. With melting values of 1640 °C and 1395 °C, respectively, NiAl and NiAl have been investigated more than $NiAl_3$, which has a melting point of 854 °C. This is reflected in the high stiffness values of 178 GPa for Ni_3Al and 294 GPa for NiAl, respectively [2]. Owing to their excellent physical and chemical properties, NiAls have been widely studied in recent decades for applications under ambient and high-temperature conditions. However, manufacture using traditional methods is hampered by their poor ductility and toughness at room temperature [3]. High fusion temperature, low density, high thermal conductance, and high hot corrosion resistance are just a few of the superior properties of Ni-Al compounds. Among them, NiAl is noteworthy because of its superior tribological properties and high Young's modulus. However, because of intrinsic limitations such as low strength, poor high temperature creep behavior, and room temperature brittleness, its industrial potential is limited. Elaboration of potential engineering applications of NiAl is limited because of these limitations [4]. Because of its high melting point and requirement of vacuum conditions, one of the most desired methods of fabricating NiAl, namely, casting, is accompanied by high costs of production. An alternative is provided in the form of powder metallurgy, which provides a promising means of fabricating nickel aluminides, combustion synthesis (CS) of which is particularly valuable as energy-conservative methods of producing intermetallic compounds. However, development of permanent AlO_3 surface oxide film during processing is a big challenge to achieving full densification of aluminides using CS in the absence of pressure application [5-8].

The SPS method has drawn much attention due to its novelty, which is tapping into effects such as Joule heating, low sintering temperature, and low sintering times. These characteristics ensure material densification is superior and effective, and hence offers clear advantage over

conventional sintering techniques. SPS has gained widespread acceptance and application for its revolutionary effect in sintering technologies since its inception [9]. One of the most popular methods of synthesizing intermetallic compounds, SPS is better than conventional casting and powder metallurgy techniques. Although having many positive effects, SPS has negligible effect on polycrystalline nickel aluminide fluidity at room temperature. The combination of mechanical activation (MA) and further treatment using SPS has been focused in recent investigations. Through causing severe plastic deformation in blends of powders, mechanical activation leads to highly dispersed composite material of high contact area and high density of internal stress, which results in superior microstructure properties for high-performance material application [10]. Sliding friction and wear tests were conducted to evaluate the bearing material potential of several nickel aluminides, Ni_3Al, alloys. Other commercially available alloys tested were IC-50, IC-74M, IC-218, IC-221, and IC-396M. Counterface materials used were: silicon nitride, nickel aluminide alloys, IC-50 and IC-396M, polycrystalline alumina, AISI 52100 steel, and M-50 tool steel. At temperatures as high as 650 °C, tests were conducted using unlubricated configurations such as ball-on-disc and oscillating geometries, with some runs being conducted with lubrication. The findings demonstrated that while lubrication decreased wear and friction for steel and silicon nitride pairs, IC-74M's wear resistance increased noticeably at higher temperatures [11]. The possibility of using intermetallic nickel aluminides (Ni_3Al) in automotive body application was explored. Ni_3Al is one of the promising lightweight material candidates for automotive body application due to low density (~ 6 g/cm^3), high temperature strength, and high oxidation and corrosion resistance. Microhardness tests in Vickers were applied to quantify mechanical properties. The thermal properties were examined using heat treatment (annealing), and properties of corrosion were examined using Tafel extrapolation experiments. The high strength and potential of Ni_3Al alloy to act as a suitable alternative material for a vehicle body is further evidenced in the increase in hardness value in terms of annealing temperature [12]. For the fabrication of nickel aluminide composites, both the techniques of planetary ball milling and powder metallurgy had effectively dispersed CNTs. In the temperature range 50-150 °C/min, bulk composites by SPS were fabricated at 800 °C, 32 MPa, and a hold time of 5 minutes. Microstructural analysis showed that increased heating rates enhanced densification to an optimal level prior to degradation. increased heating rates gave higher Vickers microhardness, which is an indication of superior mechanical properties [13]. Microstructure and mechanical properties of nanocrystalline Ni_3Al-xB ($0.0 < x < 1.5$ at%) alloys manufactured using mechanical alloying (MA) and spark plasma sintering (SPS) are explored. SEM and XRD were used to examine how crystallite size, lattice strain, and powder

Journal Pre-proof

form varied with milling time and boron addition. The results demonstrated the formation of Ni_3Al, and crystallite sizes ranging from 15 to 20 nm. The incorporation of a 0.5-1.0 at% boron increased hardness and shear strength and decreased ductility significantly [14].

Multiphase Ni_3Al-based intermetallic alloys have a difficult time deforming because of their high strength and little plasticity; they usually need to be used directly in as-cast forms or undergo straightforward high-temperature annealing. Previous studies show that high-temperature annealing (1160-1280 °C for 10 h) causes the interdendritic β phase to aggregate and coarsen without changing its volume percentage. However, the effectiveness of conventional heat treatments in refining the β phase size or volume fraction is limited [15]. Wu et al. [15] research showed that the complicated β phase compositions and precipitation types of the alloy cause its microstructure to be extremely sensitive to cooling speeds following over-solution. Laser remelting, which has cooling rates above that of water cooling, was studied for microstructural refinement to alleviate these limitations. Micro-alloyed rapidly solidified thin, surface layers can be manufactured through plasma thermally spraying carbon steel surfaces and subsequent laser melting. A CO_2 continuous laser of power 2.5 kW (operated at a power of 800 W), which creates a local molten pool with sharp temperature differences, initiates intense vortices, upon plasma spraying fine powders of nickel and aluminum onto steel. It efficiently mixes particles within milliseconds. Micro-alloyed layers of depth of 0.2 to 0.4 mm and fine pre-austenite grain size of 4 ± 2 μm are developed through rapid quenching by the cold substrate. Microhardness tests show up to triple increased hardness, which is proved to be increased mechanical strength. Under increased translation velocities, dendritic orientation, which is determined by molten pool geometry, is along the direction of the surface, which is conducive to tailored surfaces for high-performance application [16]. The effect of low-energy high-current electron beam (LEHCEB) treatment of Ni_3Al intermetallic compounds and Ni_3Al-TiC surface composites was studied using sophisticated characterization techniques. After triple surfacing, the microstructure and phases in the near-surface layer were refined by LEHCEB irradiation (8 J/cm^2, 30 kV, 10 pulses), resulting in a TiC mass fraction of 22 weight percent. Without changing surface roughness, TiC dramatically increased microhardness, wear resistance, and decreased surface crack density by 1.8 times when compared to TiC-free Ni_3Al. The results indicate how intermetallics can be optimized in engineering applications [17]. Bio-inspired composite surface structures can improve tribological performance through synergistic effects of micro-textures and solid lubricants. The performance of laser additively manufactured repaired Ni-based single-crystal superalloys is significantly influenced by γ′ (Ni_3Al) phase

morphology. Han et al. [18] discusses morphological adjustment of γ′ through heat treatment to achieve enhanced corrosion resistance. Microstructure and electrochemical analyses confirm that parts deposited in situ show better corrosion resistance than the substrate. The γ′ phase undergoes spherical to cuboidal and raft morphologies upon higher temperatures of heat treatment. The corrosion resistance is maximized to 1050 °C, which is enhanced through reduced volume fraction of γ′ and proper Cr, W, and Al distribution, and provides insight into turbine blade post-repair heat treatment.

For achieving wear and oxidation resistance in NiAl-based alloys, suitable fabrication methods should be chosen. Among different methods, including hot isostatic pressing, surfacing, and thermal spraying, one of the clean and efficient surface modification techniques is laser cladding, which provides better performance for fabricating NiAl matrix composite [19]. In twin wire and arc additive manufactured NiAl-based alloys, periodic remelting bands (RBs) containing unique microstructural properties are present. Zhang et al. studied the oxidation behavior of RB and non-RB zones in 1100 °C using Zhang et al. [20]. In RB growing epitaxially above non-RB layers, higher γ + γ′ dual-phase percentage but comparable Goss textures were present. In parabolic growth kinetics, inward AlO_3 layers, outward NiO, and intermediate $NiAlO_4$ containing scattered AlO_3 and TiO_2 resulted from oxidation. Due to increased outward cation diffusion by the γ + γ′ dual-phase, RB contained thicker oxide scales and reduced oxidation resistance. The impact of RB on pathways of oxidation was underscored by γ′ depletion under Al_2O_3, which further demonstrated differential cation transportation. Lu et al. [21] utilized ordered patterning composite (OPC) structures of SAC305 (Sn-3.0Ag-0.5Cu) and Ni_3Al alloys to produce shell-like Ni_3Al matrix composite surface structure. Using an optimal SAC305 volume percentage significantly decreased wear losses and friction coefficients, following reciprocating dry sliding tests. This was due to SAC305's self-compensatory lubricating behavior, which develops a steady-state lubricating film governed by material properties and density of surface texture. The structural support was afforded by the NiAl matrix, ensuring permanent tribological performance, while SAC305's increased energy and decreased hardness stimulated material transfer efficiently, producing transfer film. Laser cladding was employed to fabricate Cr_7C_3-based alloy cladding layers of Ni_3Al, and their microstructure and wear properties were examined. The metallurgical bonding of the cladding layer to substrate was excellent and surfaces were spotless. Microstructure comprised in situ Cr_7C_3, γ′-Ni_3Al, and β′-NiAl. The increased laser power increased heat input, which increased the size of carbides and dilution rate, changing wear properties and decreasing hardness.

Optimum wear property was attained at 2.0 kW of power, where wear rate was 0.480×10^{-5} $mm^3/N \cdot m$. The high power (2.4 kW) increased wear rate to four times and resulted in poor performance due to short, fragile rod-shaped carbides and ineffective small Cr_7C_3 particles, which encouraged adhesive and particle wear [19]. Through laser cladding of Cr_7C_3/Ni_3Al alloyed powder and Cr_3C_2/Ni_3Al mixture of powders, Cr_7C_3-reinforced composite cladding of Ni_3Al was manufactured. SEM, EDS and wear tests were utilized to examine microstructural and friction and wear properties. Cr_3C_2 was included in the mixed powder coating, while Cr_7C_3/Ni_3Al alloyed powder coating contained mainly Ni_3Al, NiAl, and in situ Cr_7C_3. The friction coefficient (0.1) and wear loss (0.75 mg) of the alloyed powder coating was less than in the mixed powder coating, and the coating possessed higher wear properties. The fine in situ Cr_7C_3 homogeneously distributed significantly improved wear properties and friction pair separation, which decreased counterpart weight loss to 42.2% [22]. In order to examine its effect on coating properties, supersonic flame spraying was utilized to produce Cr_3C_2-Al_2O_3-NiCr coating of Inconel 600. The coating was subjected to subsequent laser remelting. The coating density, metallurgical bonding, and distribution of carbides was improved, and corrosion and wear properties increased, using sophisticated characterization methods and microhardness tests. The necessity of adjustment of laser processing parameters is emphasized by the fact that increased laser power inhibited Cr_3C_2 nucleation, producing Cr_7C_3, decreased hardness, and deteriorated wear resistance [23]. An industrial CO_2 laser was employed to convert nickel-aluminide (Ni_3Al) coatings deposited on low-alloy medium-carbon steel. The ultrafine grain microstructure of the laser-treated zone was produced by fast remelting and solidification, which was determined using microstructural analysis. Wear tests in a ball-on-disc tribometer showed that wear was increased in depth, and microhardness profiling showed that increased depth of melting resulted in decreased surface hardness. The critical interplay of processing parameters to produce optimal performance was emphasized using EDS analysis, which demonstrated that migration of iron from the substrate resulted in partial dissolving of particles of Ni_3Al, which decreased surface hardness and wear resistance [24]. Selective laser melting (SLM) was employed to produce hexagonal NiAl composite reinforced using boron nitride nanoplatelets (BNNP). Though uniformly distributed BNNPs contributed to increased mechanical properties using effects like increased density of dislocation, Orowan hardening, and BNNP pull-out and bridging, in-situ developed Ni_3Al columnar grains grew in the (100) direction. The excellent tribological properties of BNNP/Ni_3Al composite were emphasized using its excellent anti-friction (coefficient of friction ~ 0.22-0.26) and wear behavior (wear

rate ~ 0.9-2.1 × 10^{-5} mm^3 N^{-1} m^{-1}), which increased by ~ 24% and ~ 51.2%, respectively, in comparison to SLMed Ni_3Al [25].

In this study, under innovative processing circumstances, the impact of laser-induced remelting on the scratch behavior of spark plasma sintered nickel aluminide alloy. In contrast to previous studies that mostly concentrate on typical atmospheric circumstances, this work applies laser surface treatments in two different gaseous environments—air and argon—in a new way. In the present study, laser power and laser scanning speed were systematically varied to alter the remelting process. Under such conditions, it became possible to conduct the deepest research on how the changes of the above-mentioned variables could influence changes in microstructure and characteristics on the surface of the alloy. Scratch tests under different loads were performed on modified areas with the purpose of evaluating scratch resistance features of the material and describe the surface behavior after treatments with a fiber laser. Therefore, this paper is of major relevance to the literature and brings some light to the contribution of laser-induced surface modifications in controlled gas atmospheres and their subsequent effects on tribological performance. In addition to improving the knowledge concerning the interaction of the processing factors with surface properties, the results also provided useful recommendations for optimizing nickel aluminide-based materials for high-performance engineering applications.

2. Modeling and Experimental Procedure

2.1. Computational method

The thermodynamic calculations were performed using the TCNI12 database and the Thermo-Calc program to estimate phase components and phase transformations, temperature and aluminum content limits of phase stability, and critical temperatures of interest in the NiAl alloy. To this purpose, a Ni-Al isopleth was calculated to map phase stability in equilibrium in various aluminum compositions and temperatures. The calculations provided important data regarding phase behavior in conditions of equilibrium, which was used to set critical phase boundaries and phase transformation temperatures.

As laser surface treatment was expected to induce remelting and subsequent solidification of the alloy surface, the material's behavior in solidification was studied. In this, the material containing 15 wt.% of aluminum was calculated using the Scheil module. The approach was applied to determine the phase sequence of transformation, reactions undergone in

solidification, and critical temperatures of the material containing 15 wt.% of aluminum in solidification.

2.2. Production of the alloy

Nickel and aluminum powders used as raw materials in the production of powder metallurgical nickel aluminide have 99.9% purity and the powders with spherical morphology are in the 2-50 µm size (Figure 1a). For the mass production of nickel aluminide, the composition ratio is determined as 85Ni:15Al wt.% and the powders are mechanically alloyed with a turbula mixer at 600 rpm for 3 h (Figure 1b). The prepared alloy powders are granulated before the cold pressing process and granule grain size is approximately 710 µm (Figure 1c). The mixed powder is initially cold-pressed prior to sintering. The resulting tablets are then positioned in graphite molds and exposed to spark plasma sintering at 1100 °C under a pressure of 40 MPa. Following this, the bulk products are annealed at 1100 °C for 60 minutes in a vacuum environment of 10^{-6} Pa. The mass material obtained after sintering has dimensions of 5x8x24 mm. According to the Archimedes principle, the density of the bulk material is determined and a successful material production with a density of 99% could be produced after the mentioned processes.

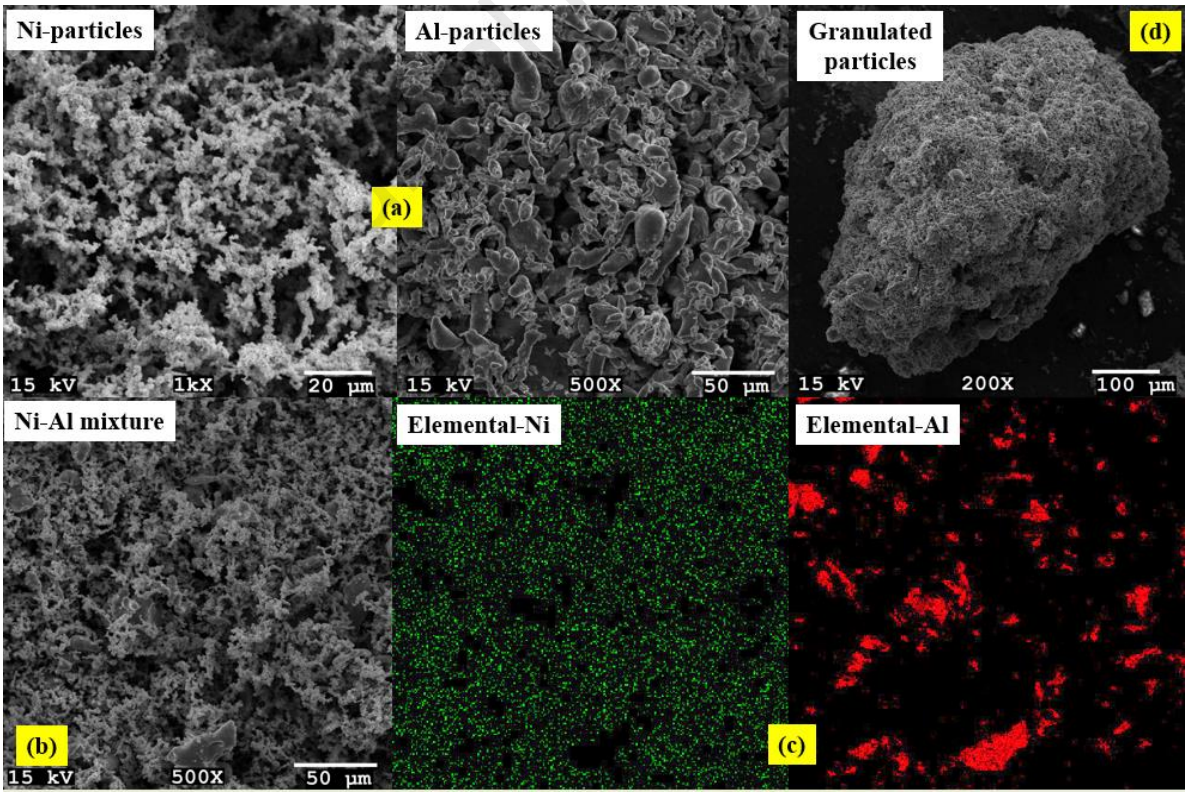

Figure 1. Images showing the used raw materials (a), distribution of elemental Ni/Al within the mixture (b and c) and granulated particles.

Journal Pre-proof

2.3. Laser treatment

In this work, samples of NiAl were treated using a fiber laser system. Generally, fiber lasers are known to exhibit high beam quality with stability and efficiency. Compact design, reduced maintenance requirements, and the possibility to generate highly focused laser beams with smaller spot sizes are only a few of the advantages. This accuracy enables the increase in energy density at the focal point-a crucial issue in material processing applications. This experiment used a 100 W fiber laser in the form of a continuous-wave laser beam. Most fiber lasers use either single-mode or multimode profile beams, which are assured of very high spatial coherence and very strong concentration of power at the core of the beam. Precise delivery of energy onto the target material with least thermal distortion to the areas surrounding it is possible by this method. The spot size depends on the focusing lens system (F-theta lens) and was optimized to get a high energy density necessary for efficient material melting and removal. In general, the wavelength of the laser used, typical of fiber lasers, is normally in the near-infrared range (~ 1064 nm), which interacts well with metallic surfaces like NiAl. The galvo head is used to direct the laser beam which then passes through the F-theta lens, which focuses it onto the surface of the nickel aluminide to create the heat affected zone (HAZ). At the focus of the beam, the energy of the laser is focused, being intense enough to melt and vaporize material. This process is further enhanced by the jets of assist gas, air or argon, which expel any ejected molten material out of the interaction zone to prevent its redeposition hence leaving a clean and clear surface. Figure 2 presents the two critical zones associated with laser-material interaction. Surrounding the molten pool is the HAZ, that area which suffers thermal gradients but which during processing is not fully melted. A recast layer forms from some of the molten material that solidifies back onto the surface. This can have a bearing on the surface finish and mechanical properties of the treated region. The molten material is thrown outwards, assisted by the gas jet, while surface debris is observed around the interaction area. The above setup was carefully optimized for consistent material processing to get minimal thermal damage with high precision. The combination of laser power, spot size, assist gas, and material properties becomes critical in determining quality and effectiveness on the surface that has been treated.

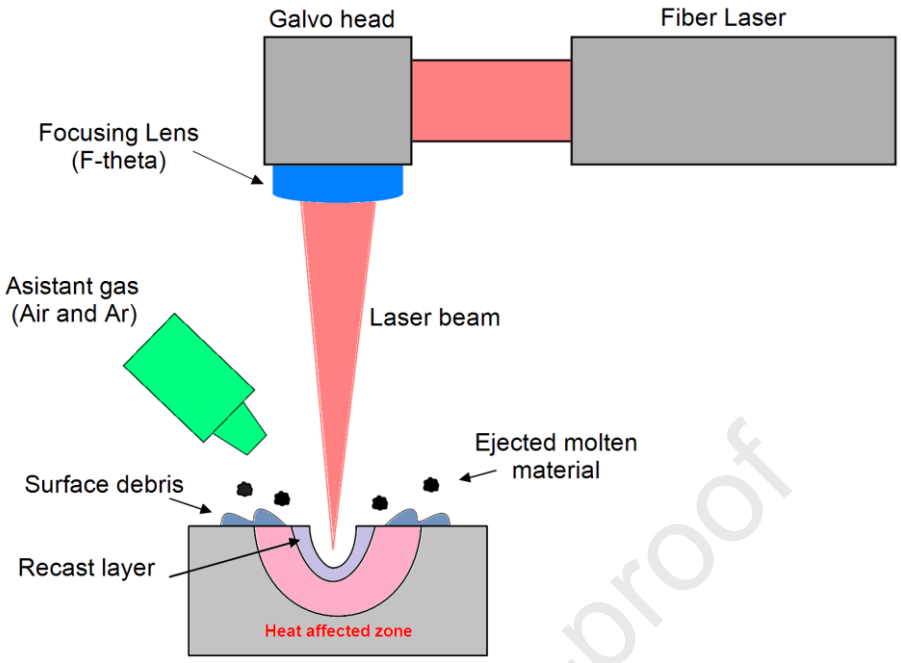

Figure 2. Schematic of the fiber laser processing system.

The experimental work summarized in Table 1 investigates the effects of varying laser power, laser speed, ambient gas and energy density on the interaction of a 100 W fiber laser with nickel aluminide (NiAl). Prior to these experiments, preliminary trials were carried out to determine the boundary conditions of the laser parameters and to ensure that the selected ranges of power, speed and energy density were optimum for NiAl processing. Using the setup shown in Figure 2, the experiments were designed to evaluate the effect of laser processing parameters on key results such as HAZ, reshaped layer formation and material ejection. The study was carried out under two ambient conditions, air and argon, to evaluate the role of auxiliary gas. As an inert gas, argon is likely to minimize oxidation and promote cleaner surface finish, while air is predicted to form oxide layers in the recast zone, affecting surface and mechanical properties. The laser power was varied at three levels (30 W, 50 W and 75 W) and the laser speed (1000 mm/s and 2000 mm/s) was adjusted accordingly to investigate their combined effects. Lower laser speeds increase the interaction time, resulting in greater thermal input, deeper melting and thicker recast layers, while higher speeds produce shallower modifications with less thermal effect. The calculated energy density (fluence energy in J/m²) further illustrates the trade-off between laser power and speed; higher energy densities (e.g. 75 W at 1000 mm/s) facilitate significant material removal but potentially cause thermal stresses, and lower energy densities allow for precise surface structuring. This systematic approach to parameter variation, as summarized in Table 1, provides valuable insight into the trade-offs between precision, thermal

damage and machining efficiency. Argon-assisted processing looks fit for applications that require smooth and oxide-free surfaces, and air processing can be considered where minor oxidation would not be a major hindrance that will involve much lower cost. Again, the versatile fiber lasers used today in material processing are identified by the study. To begin with, it has been shown from energy density and thermal effect optimization how such processes make them possible, as observed from Figure 2.

Table 1. Experimental parameters for fiber laser processing of nickel aluminide under varying ambient conditions, laser powers, and speeds.

Alloy	Ambient	Laser Power (W)	Laser Speed (mm/s)	Pulse Energy (mJ)	Influence Energy (J/m²)
A1	Air	30	2000	0,6	305
A2			1000		
A3		50	2000	1,0	510
A4			1000		
A5		75	2000	1,5	765
A6			1000		
B1	Argon	30	2000	0,6	305
B2			1000		
B3		50	2000	1,0	510
B4			1000		
B5		75	2000	1,5	765
B6			1000		

2.4. Characterization studies

After laser surface treatments, the surfaces were cleaned ultrasonically in alcohol for a long time. The surfaces were finally dried with hot air, thus ensuring that any contamination that might adhere to the surface was largely removed. Following the mentioned cleaning process, characterization of the laser-treated surfaces was carried out in two stages. The optical imaging was done in the initial process of the research study using the Evident-Olympus BX 53 MRF microscope, which was able to provide high-resolution imaging of the laser-treated surfaces. With the help of the optical microscope, these regions were probed that have already been subjected to the specified laser treatment parameters as mentioned in Table 1. Additionally, after the scratch tests, the intersection points of the scratch marks and laser treatment zones were analyzed with images obtained in the 3D imaging mode of the optical microscope. This ensured that the surfaces were initially examined for general microstructural features, and then the interaction width between the laser-induced heat input and the surface was carefully tracked

using precise 3D imaging techniques. In the second stage, topographic projections of the surfaces were monitored with 3D profilometric measurements. The surface topography assessment for laser-induced remelted spark plasma sintered nickel aluminide alloys was done using a non-contact profilometer. Parameters for scratch examination were well adjusted to analyze the craters based on high-resolution images. Scan distances included a 3.00 mm of scan distance via the X-axis and a further 5.00 mm distance through the Y-axis, with each having a step size of 5 μm. It acquired the surface roughness and scratch morphology with a very high acquisition rate of 1000 Hz. The surface topography was characterized by the Nanovea PS-50 laser non-contact profilometer, which can measure very precise and high-resolution surface topography. Besides, the measurements were made of the depth and width of the linear scratch traces, according to ISO 25178 and ISO 4287 standards. All the collected data was subsequently processed using Mountains Technology Digital Surf Software version 6.2.7487, which indeed allowed for very detailed and quite precise 3D surface profiles. A color-mapping scale was employed to map a full range of surface height distributions that covers the scratch depth and plastic deformations. It allowed the proper analysis of scratch-induced damage, since the high-resolution surface maps enable detailed 3D characterization of active damage processes involved and also disclose the remelting effects which could influence scratch behavior.

In the second stage, the characterization of the spark plasma sintered and annealed NiAl alloy was carried out with the analysis made with XRD (Rigaku Ultima +). In XRD analyses, Cu-K_α radiation is used to scan at a speed of 1°/min. in the angle range of 10-85°. The surfaces were first polished with diamond solution (3 μm) and then etched using a solution of HNO_3 (33.3 vol.%), CH_3COOH (33.3 vol.%) and HCl (33.3 vol.%) and Kalling's reagent No.2 (5g $CuCl_2$, 100 ml HCl, 100 ml ethanol) to reveal the matrix phase structure and aluminide phases distributed in the matrix, respectively. Since laser treatments are carried out under variable conditions, molten pools can exist in a certain width and depth on both surface and cross-section. In order to characterize solidification morphologies of molten pools, the surfaces and cross-sections of the alloys were examined with both light microscopy (LM, Olympus BX41M-LED) and SEM (Jeol JSM 6060). Elemental segregation during solidification and chemical content of microstructure-specific components were monitored by multiple analyses using EDS (IXRF).

2.5. Scratch Test

Scratch properties of the test specimens were made using a scratch tester according to the standard by ASTM G171-03. Figure 3 shows the setup for scratch tests. The normal loads of 5N and 15N and a speed of 2.5 mm/s were selected as the test conditions. The scratch tests were performed by taking the load perpendicular to the surface of the specimen. The spherical indenter used for this investigation was of 200 μm radius, Rockwell.

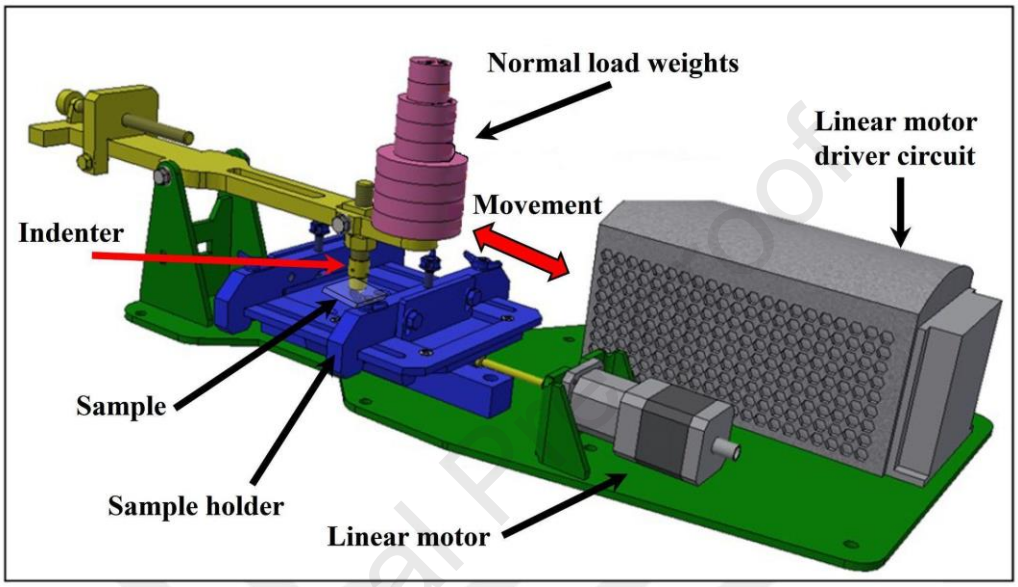

Figure 3. Scratch test setup.

3. Results and discussion

3.1. Thermodynamic modeling and microstructural characterization of the alloy

Figure 4 presents the binary Ni-Al phase diagram calculated using the Thermo-Calc software. To facilitate a clearer observation of the eutectic reaction, the eutectic region has been magnified. The composition containing 15 wt% Al is indicated by a red line on the isopleth. Phase transitions may be traced in the temperature regime of liquid to room temperature. Crystallization of phase AlNi, i.e., phase β, having BCC crystal structure, is where the process of solidification initiates. A eutectic reaction, wherein the remainder of liquid phase is converted to phases of NiAl and Ni_3Al (γ'), is observed subsequent to continued cooling. The phase of NiAl is converted to phase of Ni_3Al upon further cooling to 1100 °C, and upon further cooling to 570 °C, there is precipitation of phase of Ni_5Al_3.

The Scheil module was applied to simulate the sequence of solidification of 15 wt% Al to examine the process of solidification, and results are illustrated in Figure 5. Similar to the phase

diagram, solidification begins at 1398 °C with the nucleation of the BCC phase from the liquid. Once the NiAl phase fraction reaches 0.4 mol at 1372 °C, the remaining liquid phase transforms into a mixture of NiAl and Ni_3Al phases.

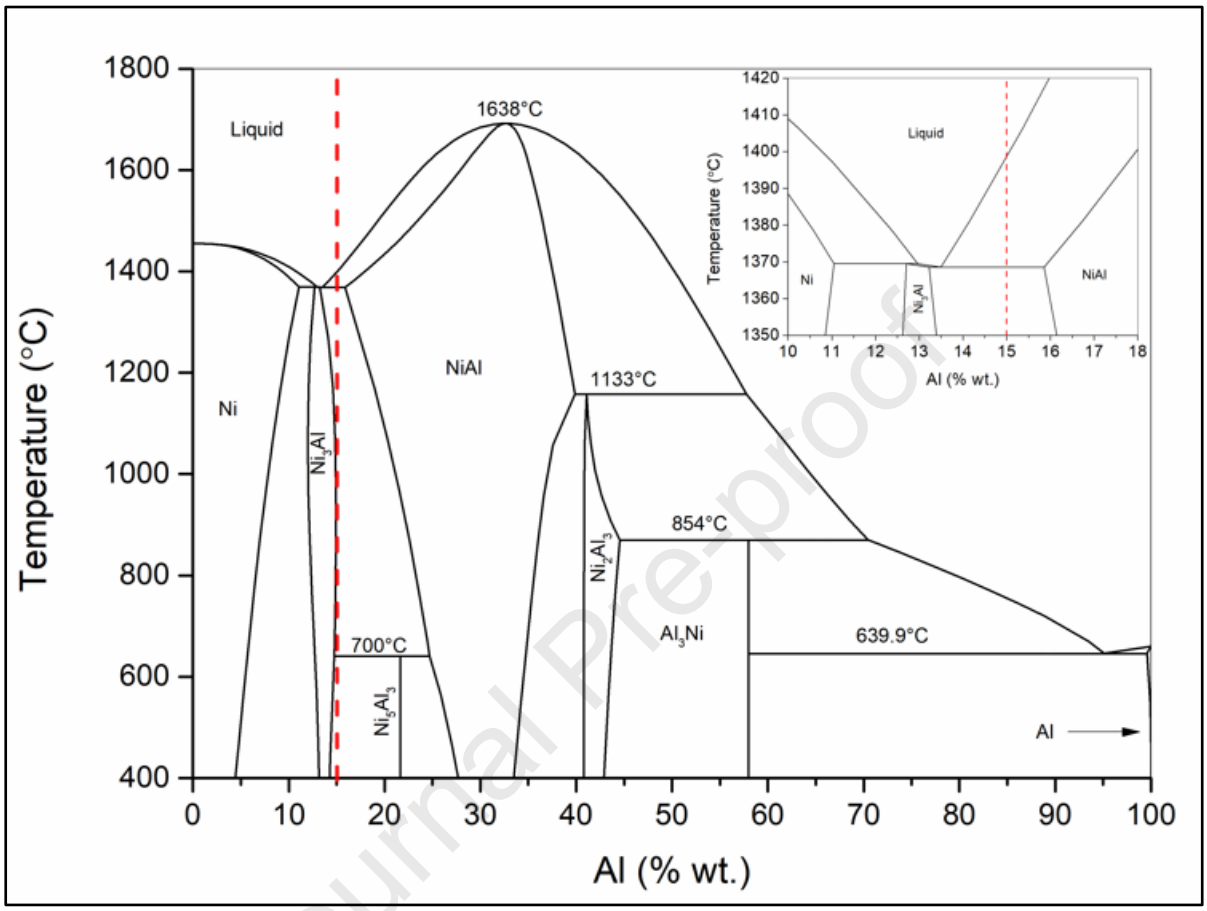

Figure 4. Ni-Al binary phase diagram calculated by Thermo-Calc software.

The molten pool is seen to experience changed alloy composition due to evaporation [26-28]. The duration and power of the laser assist in evaporating aluminum, which has a significantly lower melting temperature than nickel [29-31]. During laser remelting, aluminum may oxidize or evaporate in the molten pool, and this results in reduced aluminum content compared to in the matrix [30]. Accordingly, in view of the possibility of aluminum evaporating or oxidizing in the remelting region, the solidification behavior of alloys containing aluminum in the range of 12 wt.% to 15 wt.% was also examined. The calculated solidification curves are presented in Figure 6. For the alloy containing 12 wt.% Al, solidification starts with the nucleation of Ni, and the solidification of the remaining liquid phase is completed via a peritectic reaction forming the Ni_3Al phase (Figure 6a). For the alloy containing 12.7 wt.% Al, solidification is initiated by crystallization of γ-Ni, and subsequent nucleation of Ni_3Al from the liquid. The liquid phase and γ-Ni undergo peritectic reaction to form Ni_3Al (Figure 6b). In the alloy

containing 13 wt.% Al, solidification begins with the formation of Ni_3Al and is completed as the remaining liquid phase solidifies entirely as Ni_3Al (Figure 6c).

For the alloy containing 13.4 wt.% Al, solidification starts with the crystallization of Ni_3Al, followed by a eutectic reaction in which the remaining liquid phase transforms into NiAl and Ni_3Al (Figure 6d). The alloys containing 13.6 wt.% and 14 wt.% Al exhibit a solidification sequence similar to that of the 15 wt.% Al alloy, where solidification begins with the crystallization of NiAl from the liquid, and the remaining liquid undergoes a eutectic reaction, decomposing into Ni_3Al and NiAl phases (Figure 6e and f). Although the solidification sequence remains the same between 13.6 wt.% and 15 wt.% Al compositions, as the aluminum content increases, the amount of NiAl crystallized directly from the liquid increases, while the amount of eutectic structure (Ni_3Al + NiAl) decreases (Figure 6d-f). Additionally, as the aluminum content increases, the proportion of Ni_3Al in the eutectic structure decreases, whereas the fraction of NiAl increases (Figure 4).

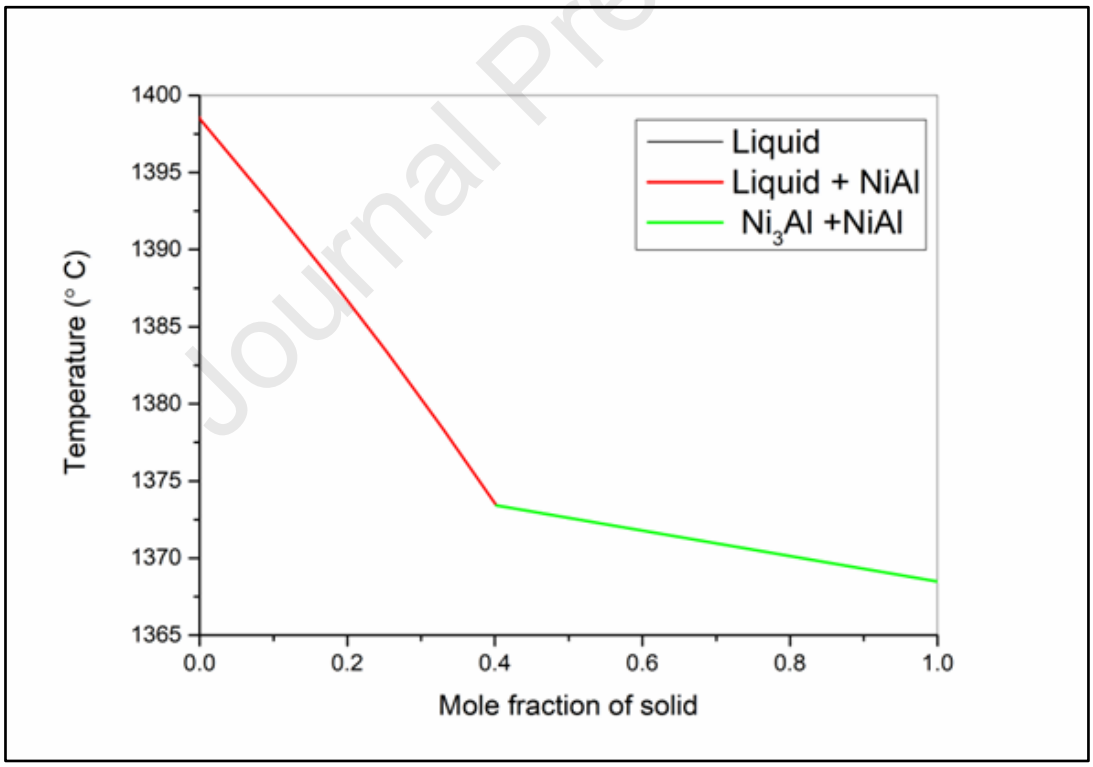

Figure 5. The solidification path of the NiAl alloy consists of 15 wt.% Al.

Journal Pre-proof

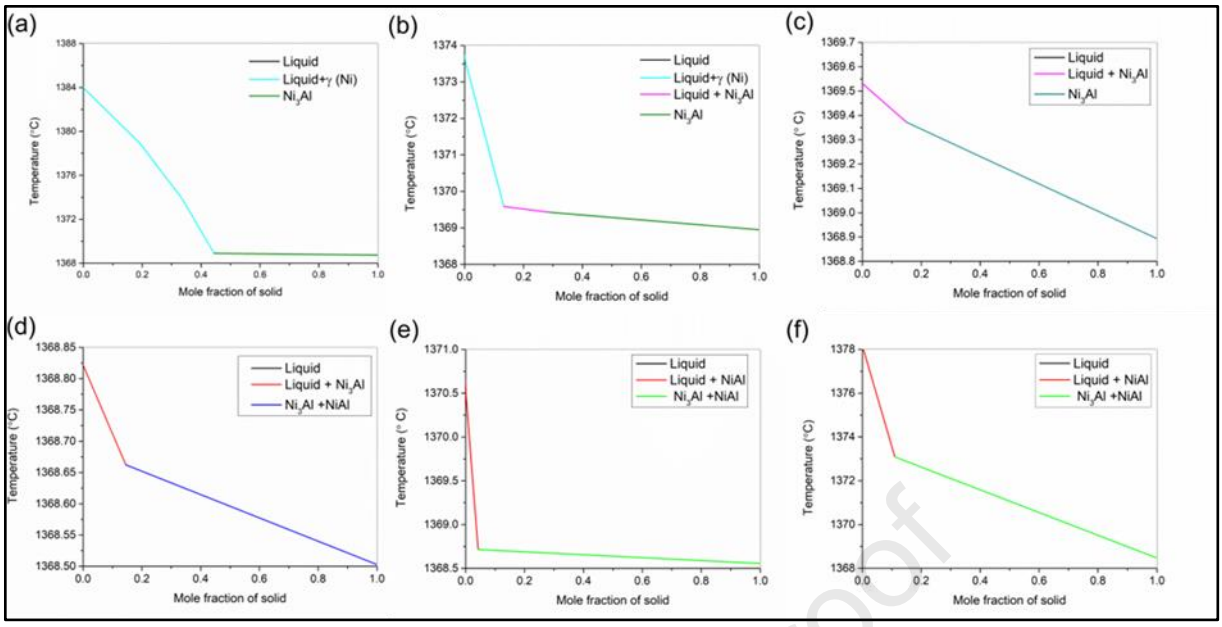

Figure 6. Solidification path of (a) 12, (b) 12.7, (c) 13, (d) 13.4, (e) 13.6 and (f) 14 wt. % Al containing NiAl alloy

Phases present in the developed alloy using powder metallurgy were characterized using XRD analysis, and the produced XRD pattern is illustrated in Figure 7. The observation is that the dominant phase present in the microstructure is Ni_3Al, indicating its high abundance in the alloy. In addition to Ni_3Al, occurrence of NiAl was also evidenced, which may indicate partial phase transformation or coexisted intermetallic compounds. In addition, although in trace quantities, there was detection of γ-Ni diffraction peaks, indicating persistence of trace quantities of the gamma-phase nickel in the structure. The observed phase distribution is in accord with thermodynamically calculated phase equilibria of this alloy composition, which is in accord with intermetallic compounds typically observed in Ni-Al systems [32-34].

In order to characterize the microstructural features of the spark plasma sintered and annealed NiAl alloy, the microstructural LM and SEM images are presented in Figures 8 and 9, respectively. The LM microstructure image reveals regions with two distinct contrasts, one bright and one dark (Figure 8a). When the bright contrast region is etched, a matrix phase with a typical FCC structure, featuring hexagonal grain boundaries and twin boundaries, becomes visible (Figure 8b). Following the XRD peaks, it is observed that the dominant phase with an FCC crystal structure is Ni_3Al (Figure 7).

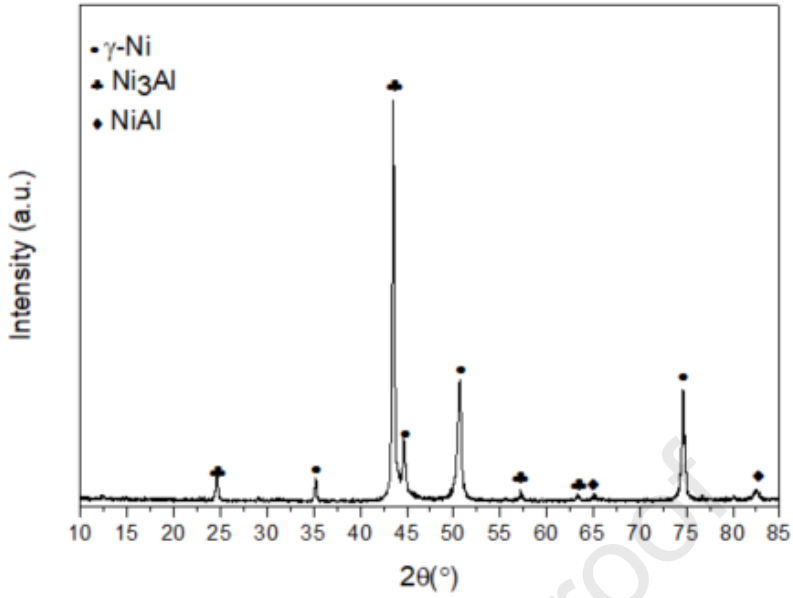

Figure 7. XRD pattern of the NiAl alloy

For the dark contrast area, this is defined to be a two-phase contrast structure in which there are two different contrast phases (Figure 8c). Judging from the results of the Thermo-Calc and the XRD pattern, this structure is identified to be a mixture of Ni_3Al and NiAl phases in eutectic form. To further analyze the microstructural components, EDS analyses were performed on the SEM images provided in Figure 9, and the obtained data are displayed on the images. The #1 EDS analysis, taken from the matrix phase, confirms that the atomic ratios correspond to Ni_3Al, indicating that this is the primary matrix phase (Figure 9). The #2 EDS of the microstructure of the eutectic area shows the phase of NiAl, and the #3 EDS confirms the presence of Ni_3Al in the eutectic region.

According to Thermo-Calc calculations, the NiAl phase, which is the phase that first precipitates from the liquid upon solidification, can convert into Ni_3Al at 1100 °C. The annealing process conducted at 1100 °C after spark plasma sintering has facilitated the stability of the Ni_3Al phase as the dominant matrix phase at this temperature. Experimental findings further confirm that through annealing, the NiAl phase can successfully transform into Ni_3Al [34-36].

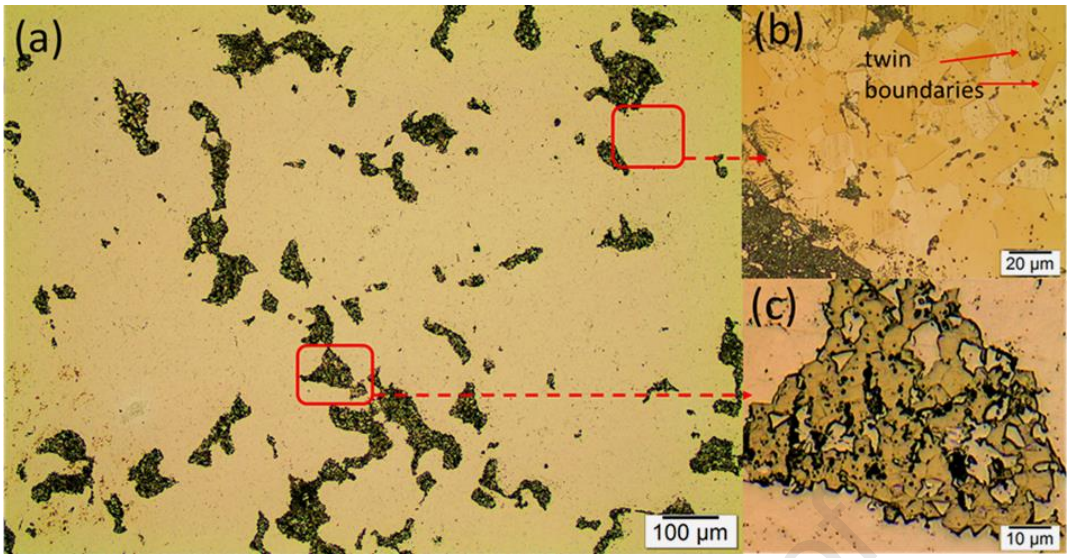

Figure 8. LM images of the NiAl alloy.

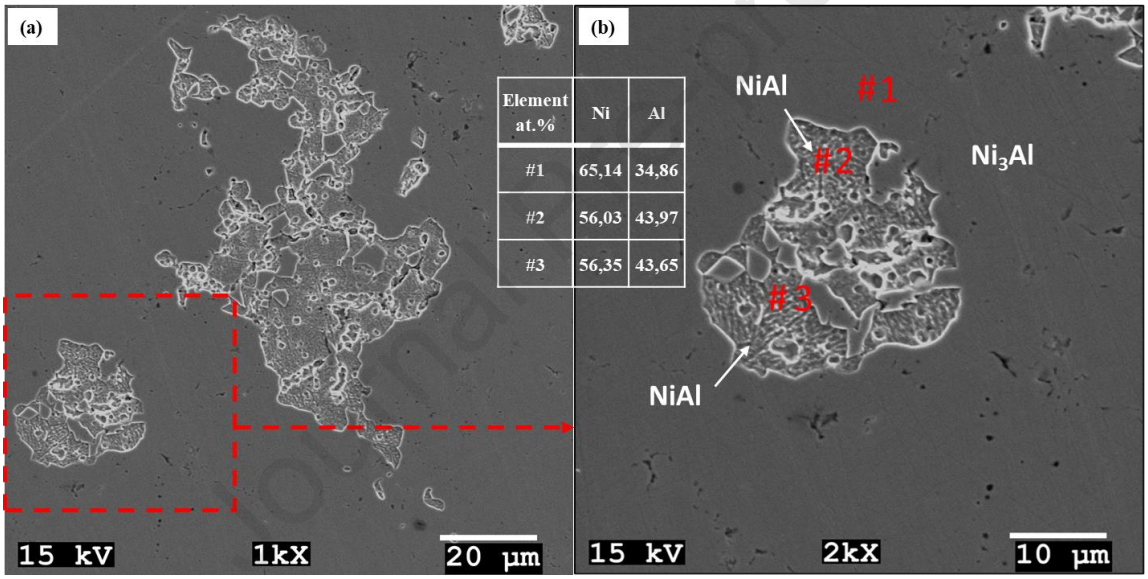

Figure 9. SEM micrographs of NiAl alloy.

3.2. Surface characterization on remelted alloy

Figure 10a shows the HAZ width of 60 µm was formed at a laser power of 30 W and a scanning speed of 2000 mm/s under air. Low pulse energy of 0.6 mJ and influence energy of 305 J/m^2 result in low thermal input. High scanning speed reduces the dwell time and restricts heat diffusion, keeping the HAZ narrow. This agrees with observations indicating the tendency of reduced thermal input to minimize excessive microstructural changes during laser processing in the nickel aluminide alloy under sintering and heating-controlled process conditions [1]. Figure 10b presents the effect of increased scanning speed to 1000 mm/s while maintaining the same laser power of 30 W in air. While increasing dwell time, the HAZ width is up to 85 µm due to the shifting of more energy in the material. The pulse energy also did not vary, being

around 0.6 mJ, but because of the input of higher heat, its HAZ has spread while compared with Figure 10a. Enlarged HAZ width corresponds to the high thermal diffusivity and localized heating conditions of SPS processed Nickel Aluminide in those studies that reported the influence of the heating rate on its microstructural evolution [37]. Figure 10c gives the 70 μm wide HAZ with the increase of laser power up to 50 W, scanning speed remaining constant at 2000 mm/s, in air atmosphere conditions. Then the higher pulse energy of 1 mJ and greater influencing energy of 510 J/m^2 will give birth to higher thermal input. Which broadens the HAZ contrary to that seen from Figure 10a. Such high scanning speeds avoid much diffusing and are similar in their fact within observatory opinions from SPS fabricated NiAl composites, since for those studied, such great input causes changes within their structure as able or suppressed under specified, modified fabrication parameters according to the desire of its manufacturing operator/machines [38]. At a similar laser power of 50 W in air, reducing the scanning speed to 1000 mm/s significantly increases the dwell time and pulse energy for a huge increase in HAZ width to 131 μm (Figure 10). The higher power then, with lower speeds, greatly amplifies the thermal effect leading to the largest extended HAZ so far. This type of behavior demonstrates the thermal sensitivity of nickel aluminide, where longer heating will result in wider diffusion zones and microstructural changes, especially for higher power conditions [39]. Figure 10e shows the HAZ width of 130 μm obtained for the laser power of 75 W and scanning speed of 2000 mm/s in air. With pulse energy of 1.5 mJ and influence energy of 765 J/m^2, substantial thermal input is delivered. Despite the high scanning rate, the wide HAZ is dominantly produced and comparable to Figure 10d due to influencing high power. Thermal conductivity and phase stability of obtained nickel aluminide for conditions have been modeled with regards to demonstrating widening effects during a laser and SPS processing [40]. Figure 10f shows a HAZ width of 118 μm obtained by maintaining the same laser power of 75 W under air but reducing the scanning speed to 1000 mm/s. Although the pulse energy was maintained at 1.5 mJ, the smaller scanning speed allowed better control over heat absorption and diffusions, which slightly reduced the width of the HAZ compared to Figure 10e. The studies on spark plasma sintered nickel aluminide confirm that the reduction of scanning speed increases dwell time, which allows higher energy absorption and, at the same time, moderate limitation of diffusion [41]. These results provide evidence of the strong impact of laser power and scanning speed on the HAZ formation under air. Indeed, lower scanning speeds systematically result in wider HAZs due to increased dwell time, whereas higher laser powers amplify the thermal effect, even at high speeds. Consequently, this is due to that interplay between laser parameter and material response-that brings precision in heat input to processes operating on the

intermetallic compounds of nickel aluminum for desirable mechanical properties to be successfully achieved [38].

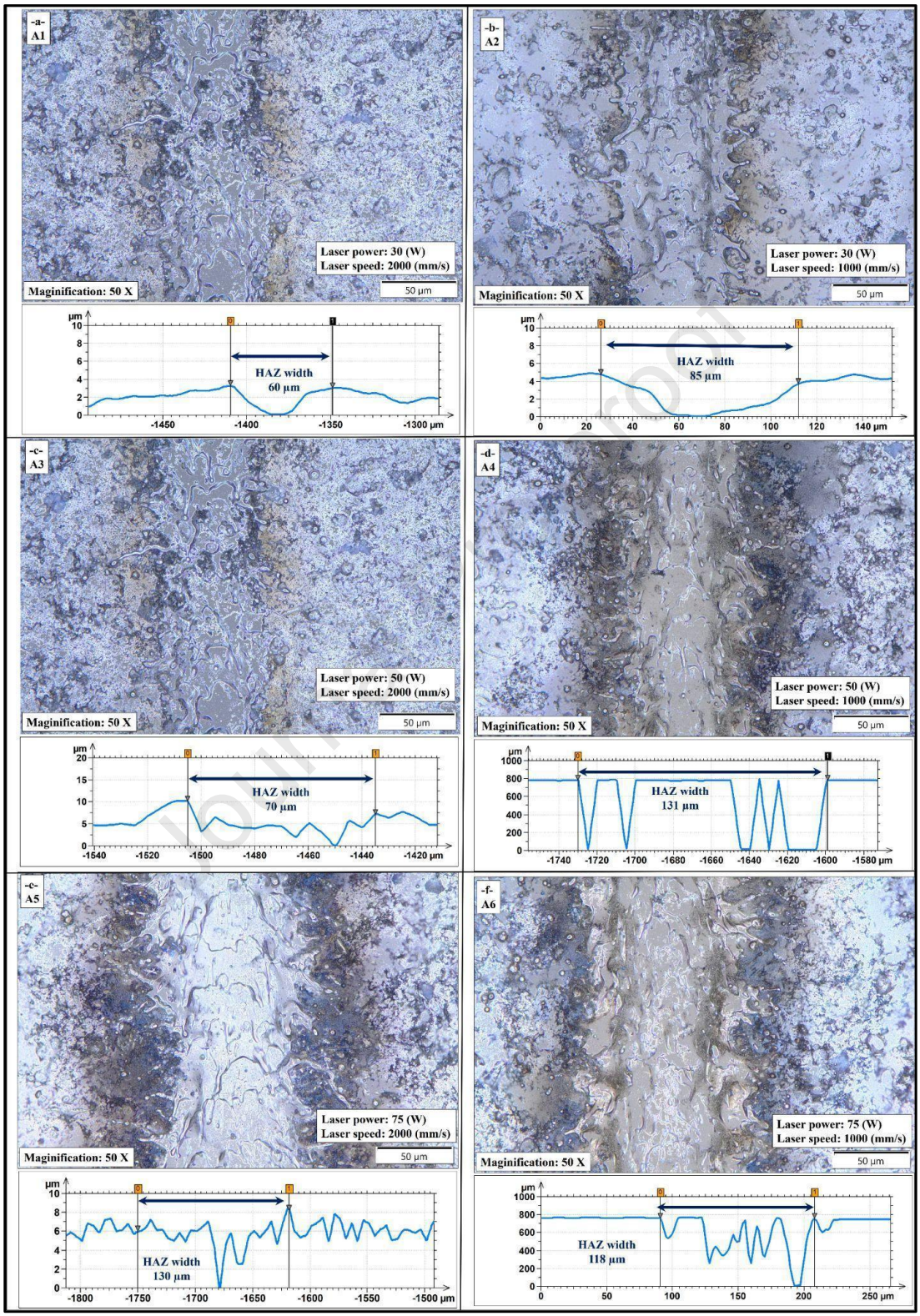

Figure 10. Optical microscope surface heat affected zone (HAZ) images of laser treated spark plasma sintered nickel aluminide alloy (a) A1, (b) A2, (c) A3, (d) A4, (e) A5, (f) A6.

Figure 11a shows the HAZ width of 58 µm formed at a laser power of 30 W and a scanning speed of 2000 mm/s in an argon atmosphere. The small pulse energy of 0.6 mJ and an influence energy of 305 J/m^2, along with the high scanning speed, result in the lowest thermal input. The argon atmosphere further reduces the heat dissipation, hence yielding a narrower HAZ compared to the air atmosphere under similar conditions. Figure 11b shows the effect of reducing the scanning speed to 1000 mm/s while keeping the laser power at 30 W under an argon atmosphere. The increased dwell time due to reduced scanning speed increases the HAZ width to 62 µm, allowing more heat transfer into the material. The argon shielding also limits the oxidation, allowing a better thermal control, which results in a slightly narrower HAZ for the same parameters compared to an air atmosphere. Figure 11c presents the HAZ width of 87 µm obtained at a laser power of 50 W and a scanning speed of 2000 mm/s under argon atmosphere. It will increase the pulse energy up to 1 mJ, increasing the influence energy to 510 J/m^2, which, in turn, makes a wider HAZ than the one shown in Figure 11a. Still, the higher scanning speed and inert atmospheric conditions of argon restrict the excessive heat diffusion, hence resulting in the generation of a moderate HAZ (Figure 11d). The consequence of using 1000 mm/s as the scanning speed with a laser power of 50 W under the protection of an argon atmosphere is depicted. Meanwhile, the width of HAZ obtained is 83 µm in an inert argon environment, which is slightly reduced compared to the HAZ formed in air condition; with the reduction in scan speed and increment of dwell time and heat input, and in an ambient, hard segments prevent the process of effective heat propagation in peripheral segments. Figure 11e, the HAZ generated width = 101 µm where laser power during treatment within the argon environment corresponded to 75 W and a scanning speed of 2000 mm/s. The pulse energy increases to 1.5 mJ, and the influence energy increases to 765 J/m^2. Under such a high scanning speed, the high laser power causes great thermal input so that the HAZ is larger compared to Figure 11c. The argon atmosphere reduces oxidation while keeping energy absorption at a high level. The width of HAZ, 109 µm obtained at laser power of 75 W for scanning velocity of 1000 mm/s under argon ambiance is shown as Figure 11f. Because the scanning speed would be quite low, heat transfer for longer periods of times and related diffusions happens more often into the substrate material. Under the argon condition, a wide HAZ is obtained because the high power results in a large amount of melting within an extended period. However, it is slightly narrower compared to its air counterpart due to the protective effects from the inert atmosphere. These observations further support that the argon atmosphere reduces oxidation and heat dissipation compared to air; therefore, narrower HAZs under similar laser processing parameters could be obtained. On the other hand, various lower scanning speeds and higher

laser powers continuously increased the HAZ width; the inert argon shielding may promote an improvement in the thermal control and surface stability in the laser processing.

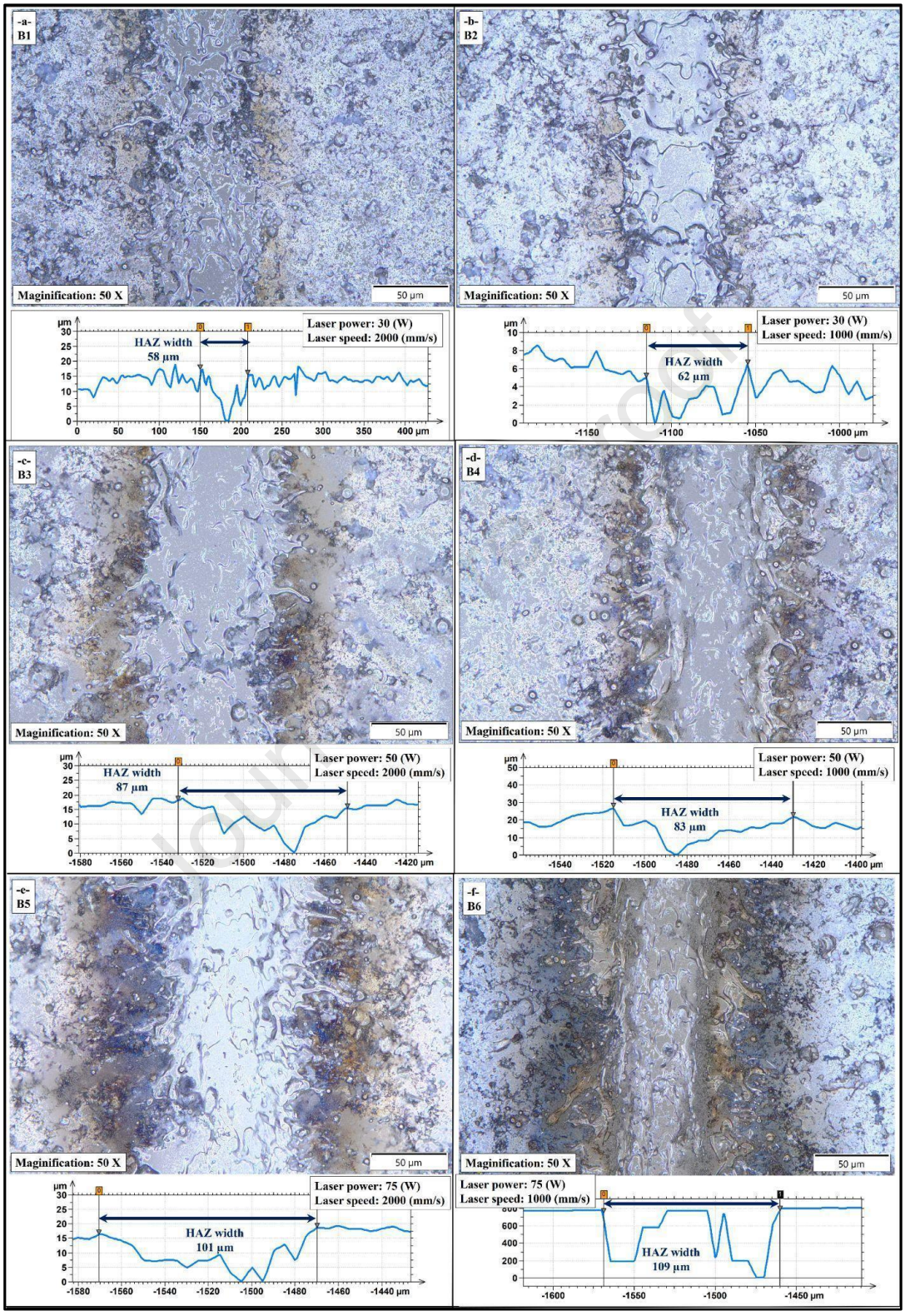

Figure 11. Optical microscope surface HAZ images of laser treated spark plasma sintered nickel aluminide alloy (a) B1, (b) B2, (c) B3, (d) B4, (e) B5, (f) B6.

Journal Pre-proof

During treatment using a laser, the focused beam of laser onto the metal surface creates a molten pool, which increases in size in the direction of beam travel [42, 43]. The molten pool is determined by interaction time and laser power, as they control the temperature of the molten pool [44, 45]. After the temperature of the alloy surface is above liquidus temperature (T_1), there is a full molten pool formed on the surface [46, 47]. Through local heat conduction in the area of molten pool, upon increased time of exposure to the laser, area above the temperature of T_1 increases, and pool increases in size [44-47]. If the laser power increases while maintaining a constant exposure time, the generated temperature rises, enlarging the area that reaches the T_1 temperature [48, 49]. The movement of the laser beam causes the molten pool to advance in the direction of the laser travel, leading to the spreading of the molten material around the pool [50, 51]. Figure 12 presents SEM-BSE images of laser-treated surfaces obtained using three different laser power levels and two laser scanning speeds under atmospheric conditions. In all surface images, HAZ, defined by the laser traces formed during processing, are observed. As can be observed in HAZ, in the direction of the laser, there is lateral spreading and flow behavior of the molten pool. Intermittent flow of molten metal, which is produced under low power of the laser and high scanning speed (A1), leads to fast solidification and clear boundaries (Figure 12a). When the scanning speed is reduced at low power (A2), the molten pool expands, the metal flow slows down, and the frequency of boundary formation decreases (Figure 12b). At high scanning speed, as the laser power increases, the width of the HAZ expands compared to the surface processed at low power (A1), and the frequency of re-melted zones decreases, although the boundaries remain distinguishable (Figure 12c and e). At low scanning speed, the higher energy input leads to a further expansion of the HAZ, causing the molten pool to cool more slowly. As a result, the solidification rate decreases, and the spacing between the solidification boundaries becomes narrower (Figure 12d and f). Upon analyzing the HAZ composition, one can see there is oxidation in the center and along boundaries of splashed molten metal. Although SEM contrast in air atmosphere does not directly indicate that oxidation is present in the laser impact zone, it is clear that there is a significant oxygen content (~ 5.3 wt.%) in the laser impact zone by considering the EDS analysis data in Figure 12b. Also, the proclivity of aluminum and nickel towards oxidation results in the prediction of the development of aluminum-rich oxides, because aluminum has higher affinity towards oxygen compared to nickel.

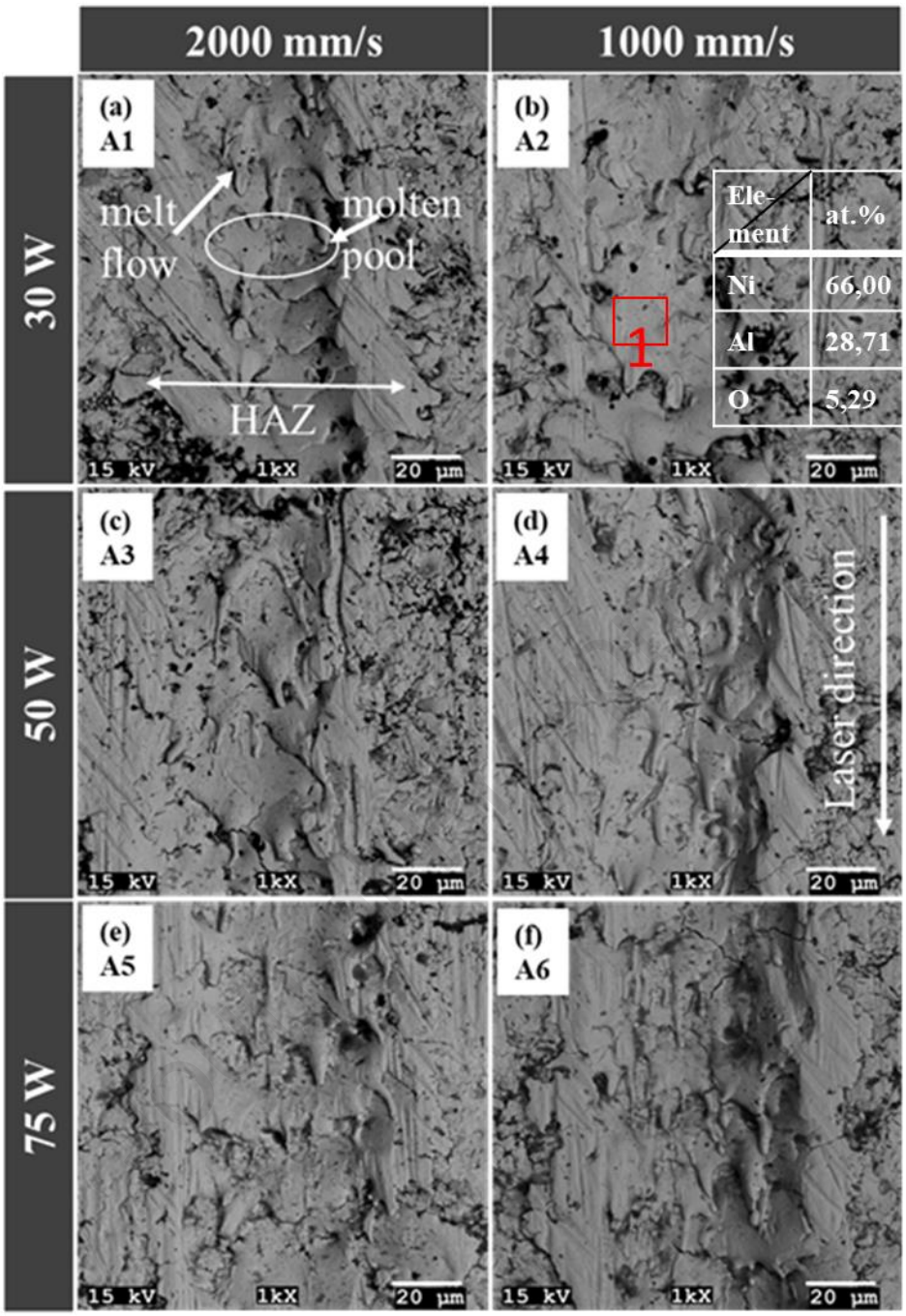

Figure 12. SEM images showing the laser treated surface of NiAl alloy under different laser power and laser speed under air condition.

The SEM images of the surfaces obtained through laser surface processing in an argon atmosphere are presented in Figure 13. The characteristics of these surfaces are similar to those obtained from laser surface processing in air, showing that an increase in laser power leads to an expansion of the molten pools and the HAZ. Likewise, as the laser scanning speed increases, the frequency of the molten pool boundaries observed within the HAZ also increases. However, a distinct difference is observed at low laser scanning speeds combined with higher laser power, where the number of molten droplets ejected and subsequently solidified increases. The argon

gas inhibits oxidation, which alters the molten material's surface energy, and this leads to an alteration of the wetting angle [52, 53]. Although there are topographic formations with similar morphologies on the surface due to laser effect, EDS data in Figure 13b reveals the effect of argon on the reduction of oxidation. The molten droplets, which are ejected, do not spread along the surface since they undergo poor wetting, and they instead solidify in droplet form. Lack of oxidation is evidenced through elemental analysis of the surfaces that have been treated, which confirms the argon atmosphere to be protective in laser treatment.

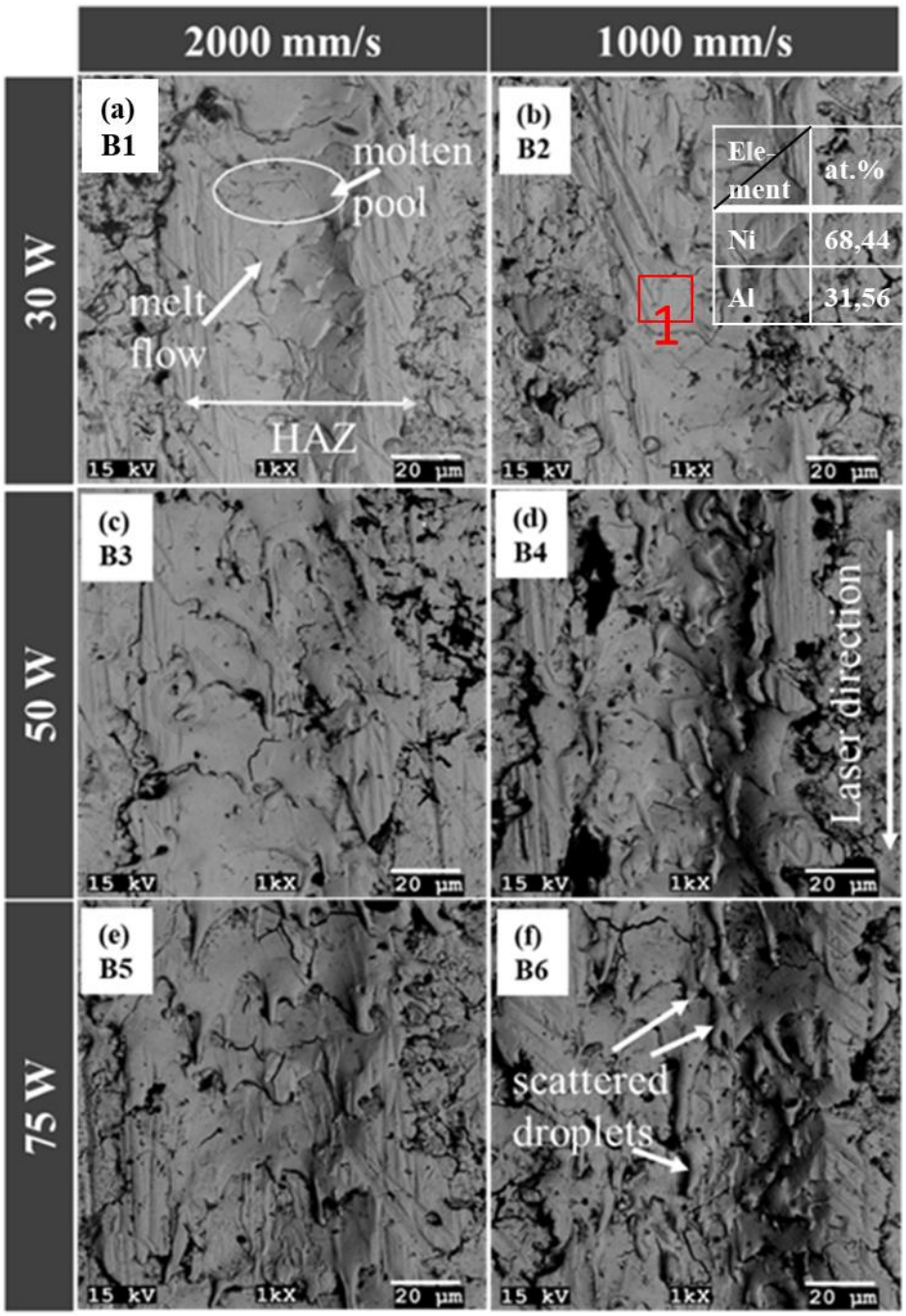

Figure 13. SEM images showing the laser treated surface of NiAl alloy under different laser power and laser speed under argon condition.

3.3. Metallurgical analyzes on the cross-section of the remelted zones

The microstructural changes induced by laser surface processing were characterized through LM and SEM analyses of the cross-sectional samples. Figures 14 and 15 present the LM images of the cross-sections. While the HAZ is observed in surface examinations as the region where melting and solidification occur, in cross-sectional analyses, this melted and solidified region appears just beneath the surface in the form of a semi-circular remelted zone (RZ). When the laser beam interacts with the surface, the underlying remelted and solidified region forms in a semi-circular shape. At the point of laser incidence, the temperature reaches its peak, and heat propagates hemispherically into the material. Due to thermal conduction, the molten zone is more concentrated at the center, while the temperature gradually decreases toward the edges [54, 55].

As the temperature of the alloy surface exceeds its liquidus temperature (T_1), a molten pool is formed [56, 57]. The heat is symmetrically conducted beneath the surface, and as thermal dissipation occurs between the molten pool and the matrix, the pool solidifies from the center toward the edges, forming a semi-circular morphology [54, 55]. As the laser beam moves, the molten pool follows, creating a continuous track on the surface [50]. However, due to the radial heat distribution beneath the surface, the remelted zone consistently retains its semi-circular shape [56, 57].

Laser processing parameters directly influence the width and depth of the remelted zone [42-51]. In air atmosphere, at all laser power levels, reducing the scanning speed (1000 mm/s) results in an expansion of the remelted zone in both width and depth (Figure 14). Additionally, an increase in laser power, regardless of scanning speed, leads to further broadening and deepening of the remelted zone (Figure 14). The deepest and widest remelted zone was observed in sample A6, which was processed at the highest laser power and lowest scanning speed (Figure 14f). Similarly, in argon atmosphere, the remelted zone follows the same trend, where a decrease in scanning speed and an increase in laser power lead to a larger molten region (Figure 15). The deepest and widest remelted zone in argon atmosphere was observed in sample B6 (Figure 15f). IM images reveal that, in both air and argon atmospheres, the remelted zone exhibits a different microstructural composition than the matrix, maintaining its semi-circular morphology (Figures 14 and 15). Microstructural investigations indicate the presence of NiAl and Ni_3Al eutectic structures within the remelted zone (Figures 14 and 15). To confirm the solidification characteristics, the cross-section of sample A1 was analyzed through SEM-EDS,

revealing that the remelted zone is composed of a eutectic mixture of Ni_3Al and NiAl (Figure 16).

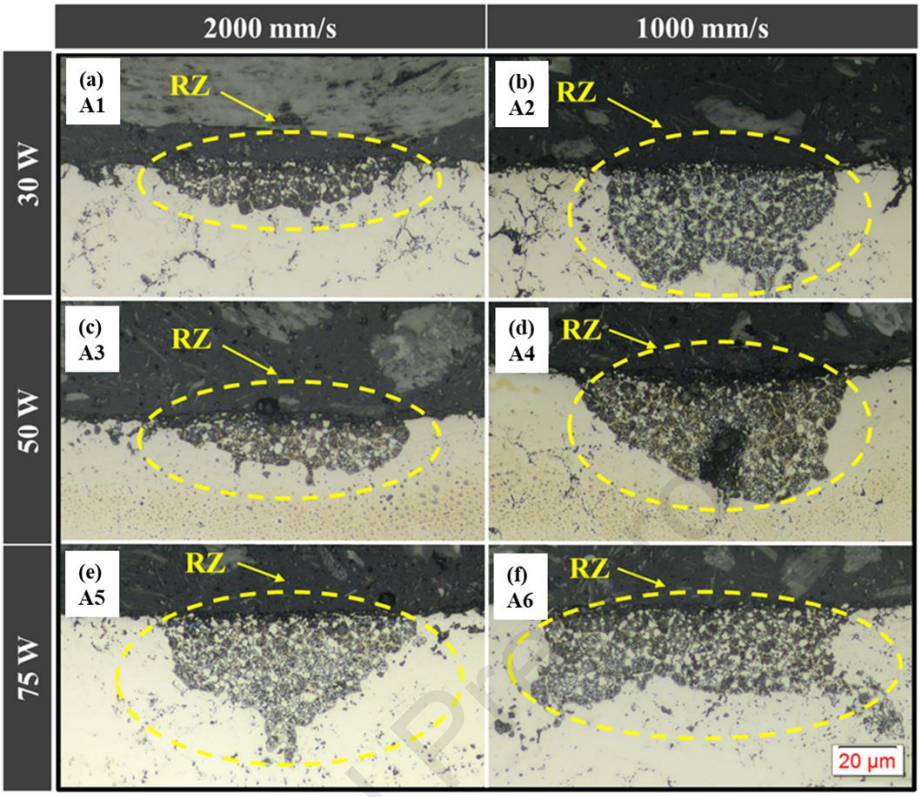

Figure 14. LM images showing the cross-sections of the laser-treated nickel aluminide alloy under air condition.

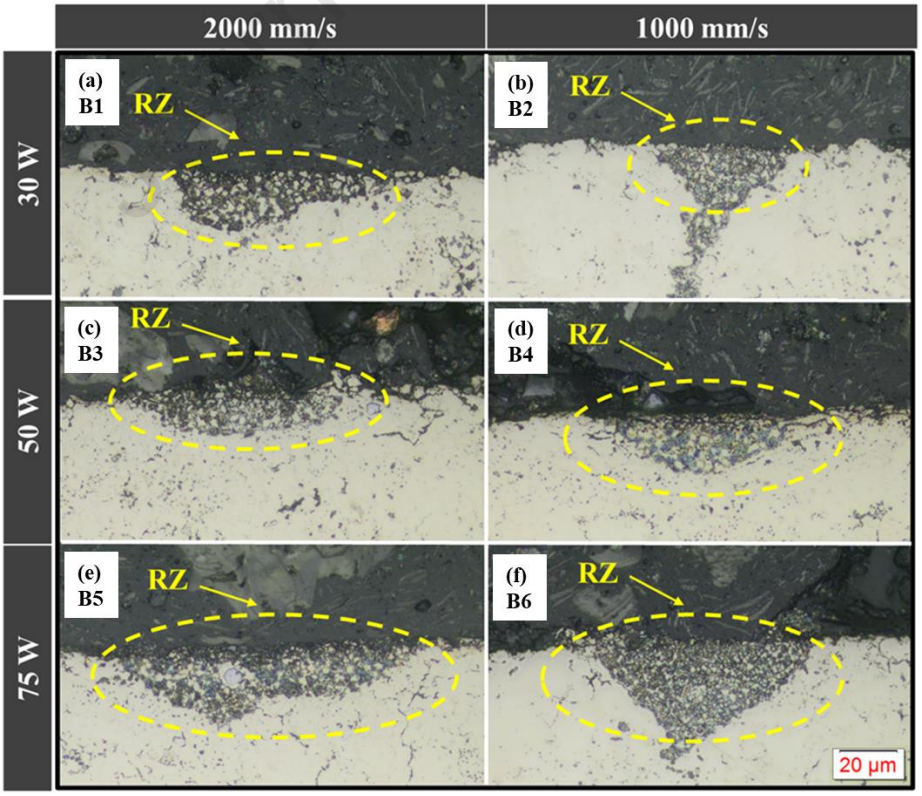

Figure 15. LM images showing the cross-sections of the laser-treated nickel aluminide alloy under argon condition.

During laser processing, as the molten region remains in the liquid phase, the following transformations occur: elemental segregation between the matrix and the molten region, elemental evaporation along the exposed surface of the remelted zone, and alteration in phase stability due to chemical composition variations [30, 42]. These processes lead to local chemical inhomogeneities, modifying the solidification characteristics of the remelted zone [32]. Since chemical composition and temperature are the two critical parameters governing phase stability via Gibbs free energy changes, any variations in composition during solidification alter the stable phases within the remelted region [58, 59]. Of course, in the resolidification zone all metallurgical variables will have a significant effect on the load carrying capacity of the material. In this case, the crystallinity and crystallite sizes in the solidification structure, the elemental distribution caused by segregation and the possible phases must be characterized with metallurgical analysis. Although the phase variation caused by segregation in most solidification processes and the amount, distribution and composition of these phases directly determine the material properties, it is also possible that local thermal activations, especially caused by laser, cause partial evaporation in the material and, as a result, a localized decrease in the concentration of solute solution hardening elements. In order to follow elemental variations within the remelted zone, EDS line/mapping analyses were performed on A1 (air atmosphere) and B1 (argon atmosphere) samples processed under identical laser parameters. The SEM images and EDS line profiles and mappings of these samples are provided in Figures 17 and 18, respectively. EDS mapping indicates relatively homogeneous distribution of nickel and aluminum in the melted and resolidified zones. However, it is inevitable that there will be a change in the temperature gradient and interfacial morphology at the liquid-solid interface due to the variable local heat input and process atmosphere. Although microscopic examinations do not indicate a significant change in solidification morphology, it is possible that elemental concentration changes occur as a result of segregation or local evaporation during terminal and lateral interface movement. The horizontal EDS line scan of the remelted zone in A1 (air atmosphere) reveals a gradual decrease in aluminum content, reaching its minimum at the center of the remelted zone, while nickel content remains relatively unchanged (Figures 17a and b). Similarly, in the vertical scan, aluminum concentration remains lower throughout the remelted zone compared to the matrix (Figures 17c and 17d). The oscillations observed in the aluminum profile correspond to the presence of aluminum-rich Ni_3Al phases within the remelted zone. Likewise, in the argon-processed sample B1, the EDS line scan along the horizontal axis indicates a reduction in aluminum content, while nickel remains relatively stable (Figures 18a and b). The vertical EDS line scan also confirms lower aluminum levels in the

remelted zone compared to the matrix (Figures 18c and d). Laser energy density plays a key role in determining aluminum evaporation rates in NiAl alloys during laser remelting and the localized decrease in concentration of aluminium, which makes a significant contribution to solid solution hardening, may allow the surface to be further scratched if subjected to any nominal load. Higher energy densities result in elevated melt pool temperatures, intensifying aluminum evaporation due to its lower boiling point (2519 K) compared to nickel (3186 K) [60, 61]. Studies on Laser Powder Bed Fusion (LPBF) and Directed Energy Deposition (DED) have demonstrated that excessive laser power or slow scanning speeds lead to localized overheating, resulting in significant aluminum loss, which in turn modifies alloy composition and degrades mechanical properties [62, 63]. A controlled energy input is essential to prevent undesirable phase transformations and porosity formation, as demonstrated in recent studies on thermal field-assisted laser processing [64]. Additionally, investigations on aluminum evaporation have shown that increasing laser energy density enhances Marangoni flow, influencing the melt pool stability and redistribution of aluminum-rich phases [65]. EDS profiles in Figure17 and Figure 18 also indicate the presence of oxygen solubility or possible internal oxidation within the melt pool of variable atmospheres. In a laser process exposed to air atmosphere, a considerable oxygen content is observed in the remelting and solidification pool, especially along the longitudinal section (Figure 17). However, it has also been determined that if an inert gas atmosphere such as argon is created, there is no significant oxygen content in the equivalent cross section (Figure 18). Such a finding indicates that process-induced oxidation is significantly reduced.

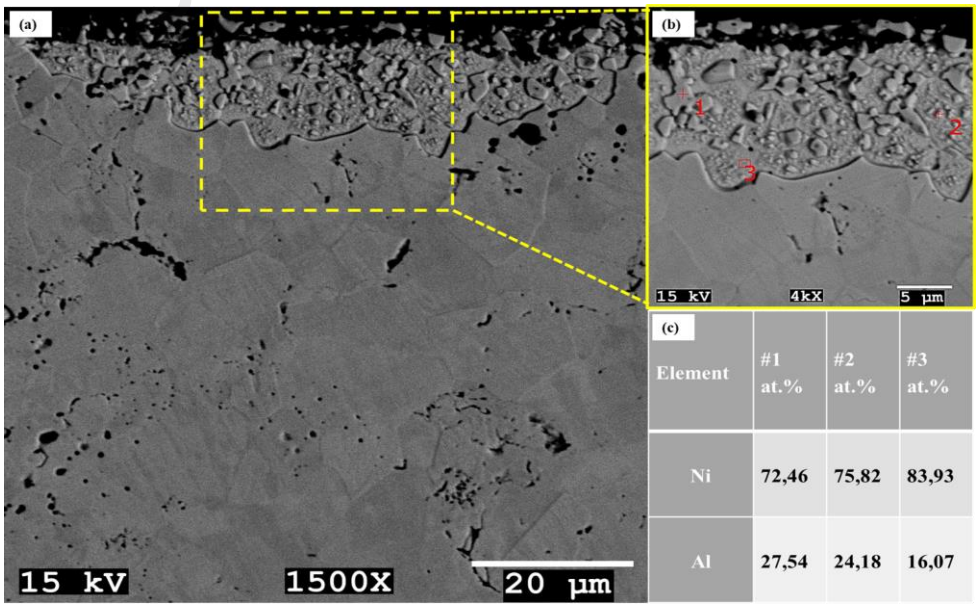

Figure 16. SEM-EDS analysis of A1 sample.

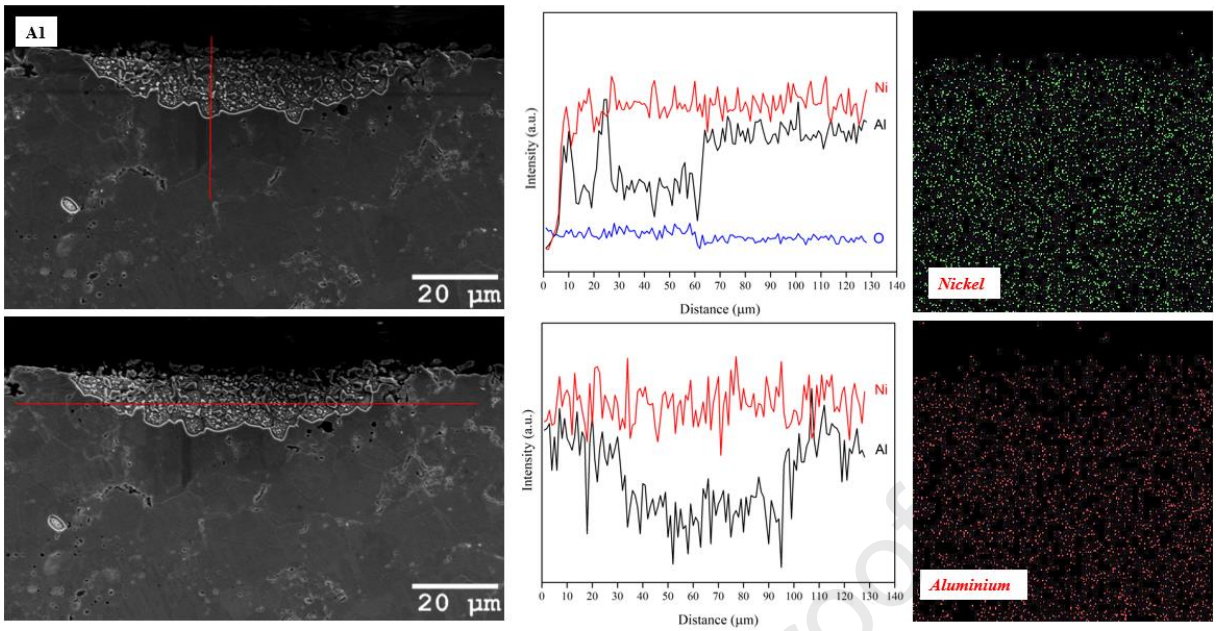

Figure 17. SEM micrographs and EDS mapping and line scan profiles of the laser-treated spark plasma sintered nickel aluminide alloy; A1

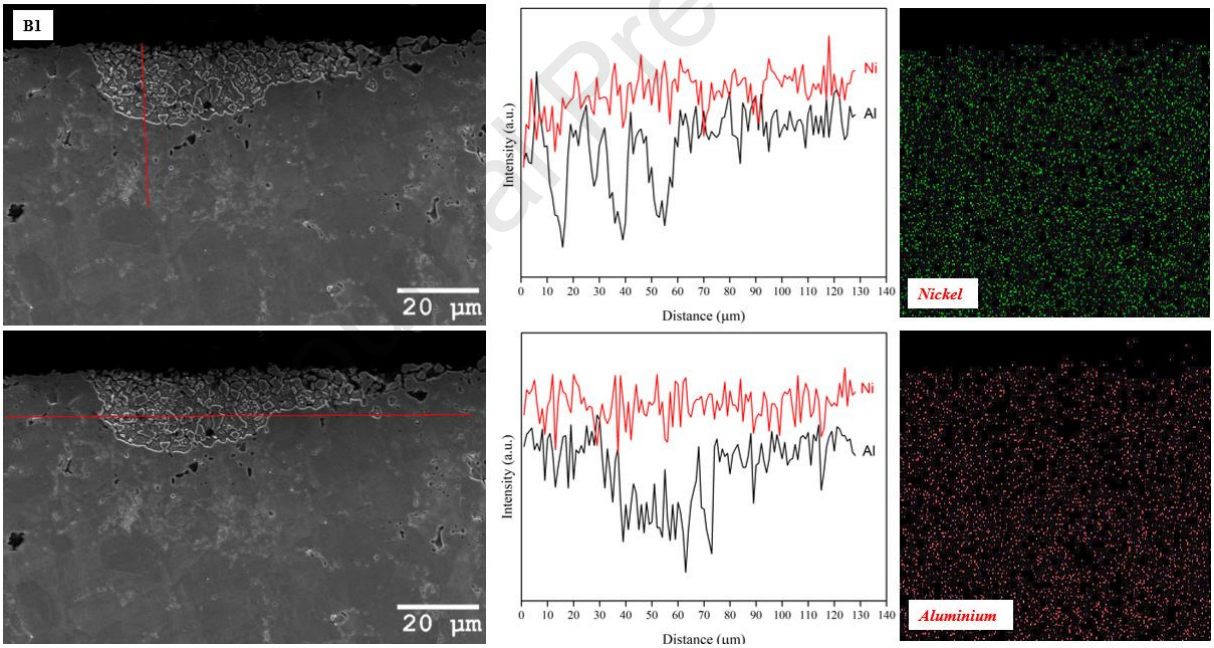

Figure 18. SEM micrographs and EDS mapping and line scan profiles of the laser-treated spark plasma sintered nickel aluminide alloy under different processing conditions; B1.

3.4. Scratch behavior of the modified surfaces

Scratch tests were conducted under two different loads on the surfaces of laser-treated specimens. The LM images of the scratch tracks obtained from tests conducted under a 5N load for specimens treated under air and argon atmospheres are provided in Figures 19 and 20, respectively. The scratch tests were initiated from the untreated surface of the specimens and progressed perpendicular to the laser traces. In Figure 19a, the laser trace is defined as the HAZ, and the corresponding scratch track is shown. Upon examining the scratch tracks of specimens subjected to laser treatment in air, it was observed that the scratch test produced a smooth track along the rough material surface. Studies on laser surface modification have shown that such treatments improve wear resistance by altering surface roughness and phase distribution, leading to more uniform scratch patterns [66, 67]. During the scratch test, as the indenter moved across the untreated surface, it scratched the surface, displacing material, which was then re-adhered along the track or at the track edges in the form of adhesive layers. When the indenter reached the HAZ, the morphology of the smooth track changed, and the displaced material accumulated in front of the indenter adhered to the HAZ, causing an interruption in the scratch track along the laser traces (Figure 19). This discontinuity varies in spacing depending on the distance between the adhesive layers. In Figure 19a, this discontinuity is referred to as the adhesive layer boundary.

The difference in response to the scratch indenter between the untreated alloy surface and the HAZ region arises from the distinct microstructural characteristics of these two regions. Studies have shown that NiAl and Ni_3Al phases exhibit different mechanical behaviors, where Ni_3Al, with an FCC crystal structure, has higher plastic deformation capability, whereas NiAl, with a BCC structure, is harder and less ductile. The untreated alloy possesses a Ni_3Al matrix with a face-centered cubic (FCC) crystal structure, which has high plastic deformation capability [68, 69]. A matrix with such characteristics can easily deform under load and re-adhere to the surface in the form of adhesive layers [70]. The NiAl phase, present in the eutectic structure within the HAZ, has a body-centered cubic (BCC) crystal structure, making it harder and less capable of plastic deformation. The formation of a NiAl-Ni_3Al eutectic structure within the HAZ results in the laser-treated regions being harder and exhibiting lower plastic deformation capability compared to the matrix [71]. The increase in HAZ width and depth leads to a larger area resistant to indentation during the scratch test. When analyzing the intersection of the scratch track with the HAZ, it is evident that as the HAZ width increases, the spacing between the accumulated adhesive layers on the HAZ also increases. Literature indicates that HAZ width

correlates with increased hardness, which in turn influences tribological properties, such as wear resistance and adhesion strength, under high loads [72]. The A6 specimen, which has the widest HAZ, exhibits the largest spacing between these accumulated layers (Figure 19f).

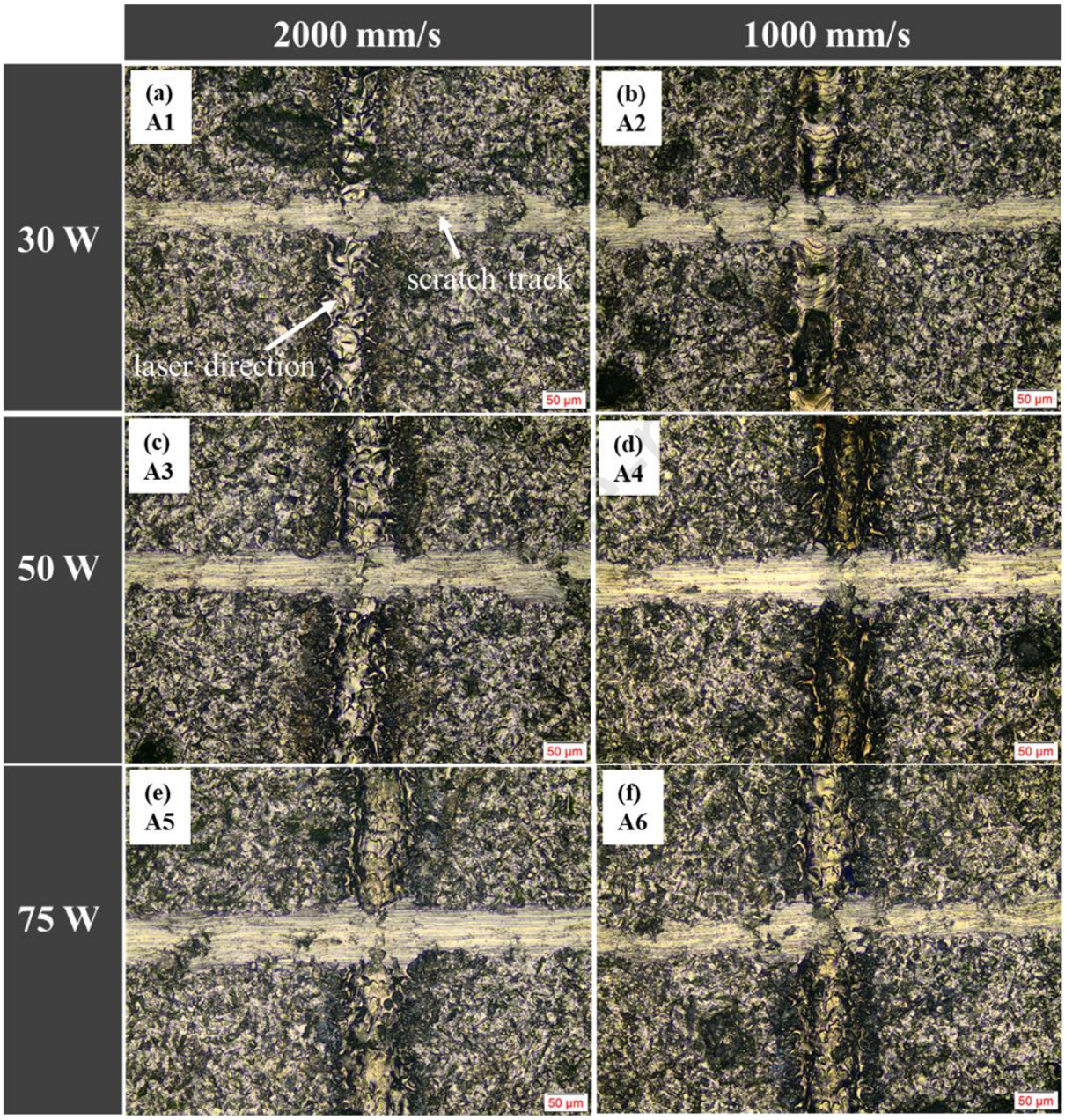

Figure 19. LM images showing the scratched surfaces of laser treated NiAl alloy under air condition obtained after scratch tests under 5N load.

Scratch tests performed on laser-treated specimens under an argon atmosphere yielded similar scratch track characteristics (Figure 20). However, the spacing between adhesive layers adhered to the HAZ was wider compared to specimens treated in air. Notably, in laser treatments performed at the highest power, the spacing between adhesive layers formed on the HAZ reached significantly greater values than those in the air-treated specimens (Figures 20e and f).

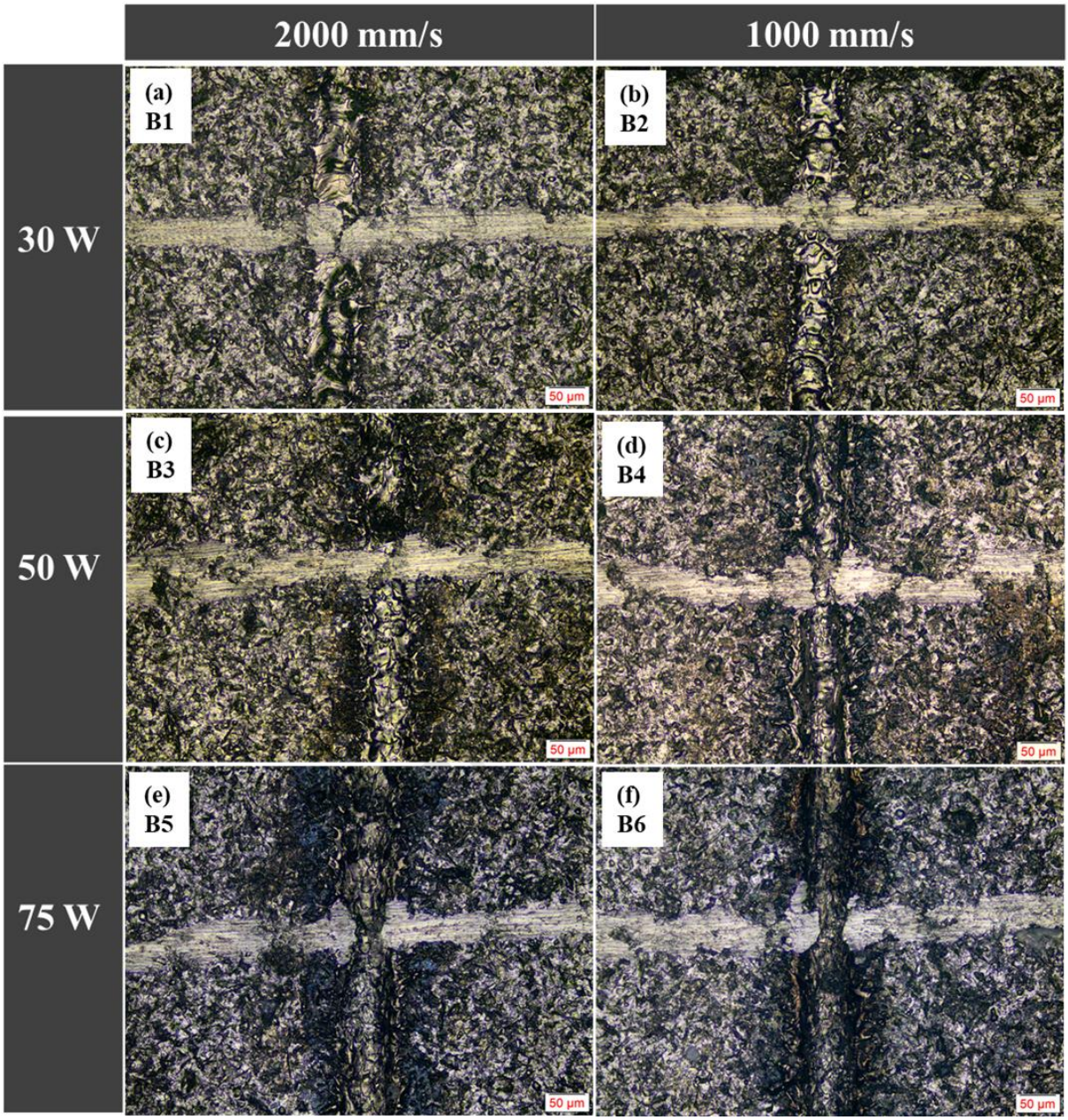

Figure 20. LM images showing the scratched surfaces of laser treated NiAl alloy under argon condition obtained after scratch tests under 5N load.

In an argon atmosphere, aluminum oxidation or evaporation from the molten pool occurs at a lower rate compared to air. A reduction in aluminum content leads to an increase in the amount of soft Ni_3Al within the eutectic structure, while the proportion of hard NiAl decreases (Figure 4). This finding is consistent with prior research, which has demonstrated that argon shielding during laser processing enhances phase stability and minimizes oxidation-induced defects, thereby improving surface wear performance [73]. Consequently, the molten pool formed in an argon atmosphere contains a higher proportion of NiAl compared to air, resulting in a relatively

harder molten pool. The laser-treated surface in an argon atmosphere inherently exhibits greater resistance to indentation during the scratch test, making increased resistance to indenter penetration inevitable.

The LM images displaying the scratch tracks obtained after scratch tests conducted under a 15N load are presented in Figures 21 and 22. The scratch tracks formed under 15N load on all specimen surfaces are wider compared to those obtained under 5N load. The increase in applied load resulted in greater penetration of the scratch tester indenter into the surface, leading to the formation of wider tracks. This observation aligns with previous studies, which have shown that higher applied loads in scratch testing increase contact stress, leading to deeper penetration and enhanced plastic deformation in alloys having fcc matrix [74]. Throughout the scratch test, a smooth track was formed on the surface, with fine abrasive scratches and accumulated material at the track edges, which resulted from plastic deformation. Similar results have been reported in tribological studies, where laser-treated surfaces exhibited abrasive wear mechanisms accompanied by plastic deformation due to increased stress at the scratch contact zone [75, 76].

Upon examining the intersection between the scratch track and the HAZ, it was observed that in sample A3, laser-processed at 1000 mm/s scanning speed and 50 W power under air atmosphere, the adhesive layer on the HAZ exhibited fracture at its boundary (Figure 21d). Similarly, samples A4 and A5 also displayed fracture within the adhered layer on the HAZ (Figures 21e and 21f). These fractures indicate localized stress concentrations due to load-induced plastic deformation, which leads to the failure of the adhesive layer at the HAZ interface. Previous research on laser-modified NiAl-based intermetallics has shown that such fractures often initiate at the interface between eutectic phases, where stress accumulation occurs due to differences in plasticity and hardness [77].

Similar scratch track characteristics were observed in argon-processed samples, where fracture in the adhesive layer was particularly evident in samples processed at 50 W and 75 W laser power (Figures 22c-f). The HAZ region in these specimens exhibited increased resistance to plastic deformation, as demonstrated by the fracture of the adhesive layer caused by the scratch indenter. The increase in applied load (15N) further intensified the stress state, leading to enhanced plastic deformation at the scratch track–HAZ interface, which is evident from the fracture propagation along the adhesive layer. Prior studies eutectic structures have demonstrated that laser-induced microstructural changes significantly impact deformation

behavior, particularly under high indentation loads, where phase boundaries act as stress concentrators, influencing crack initiation and propagation [76, 77]. This confirms that higher indentation loads not only increase the scratch width but also amplify the material's plastic response, particularly in laser-processed regions where microstructural variations influence mechanical behavior.

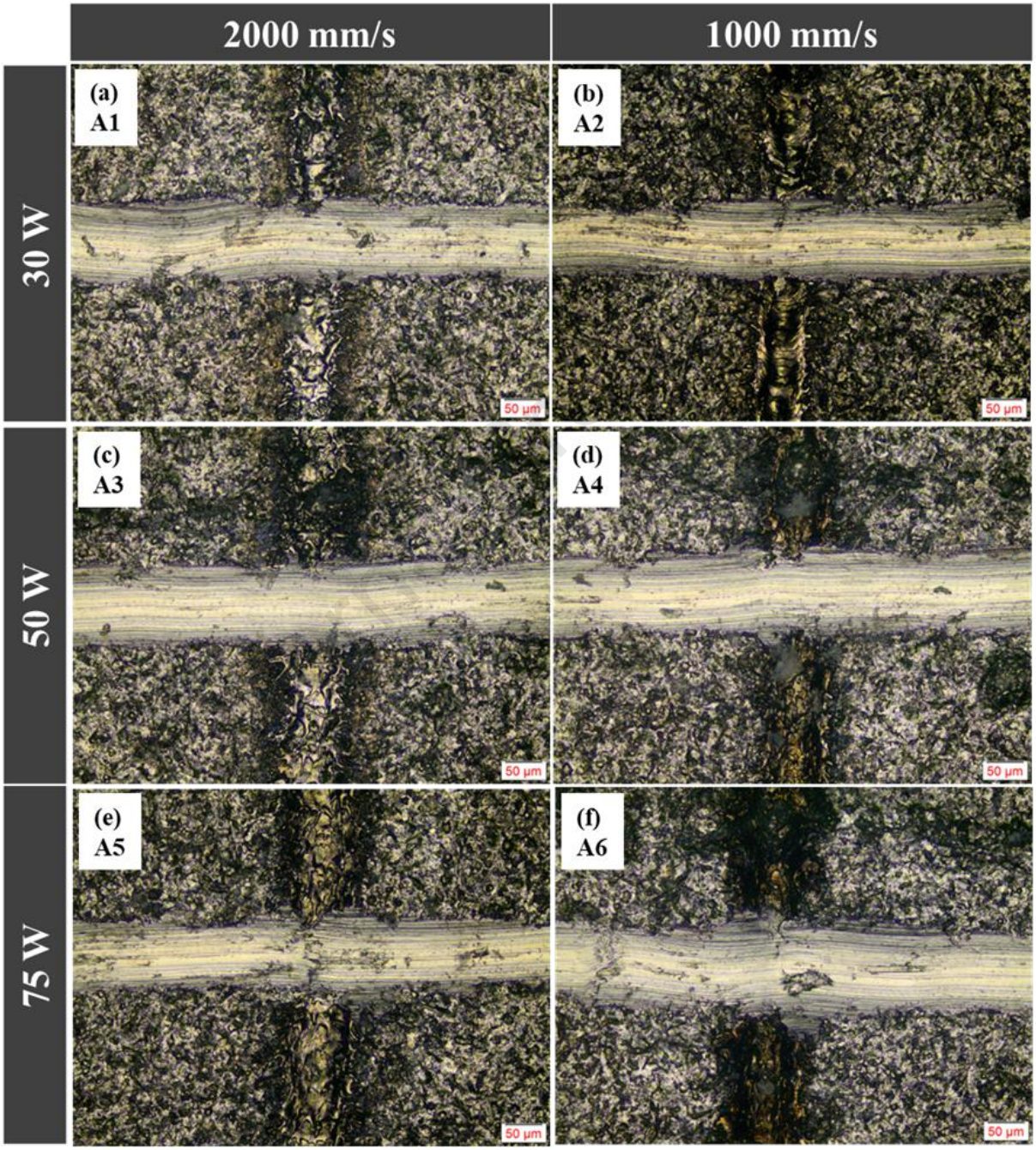

Figure 21. LM images showing the scratched surfaces of laser treated NiAl alloy under air condition obtained after scratch tests under 15N load.

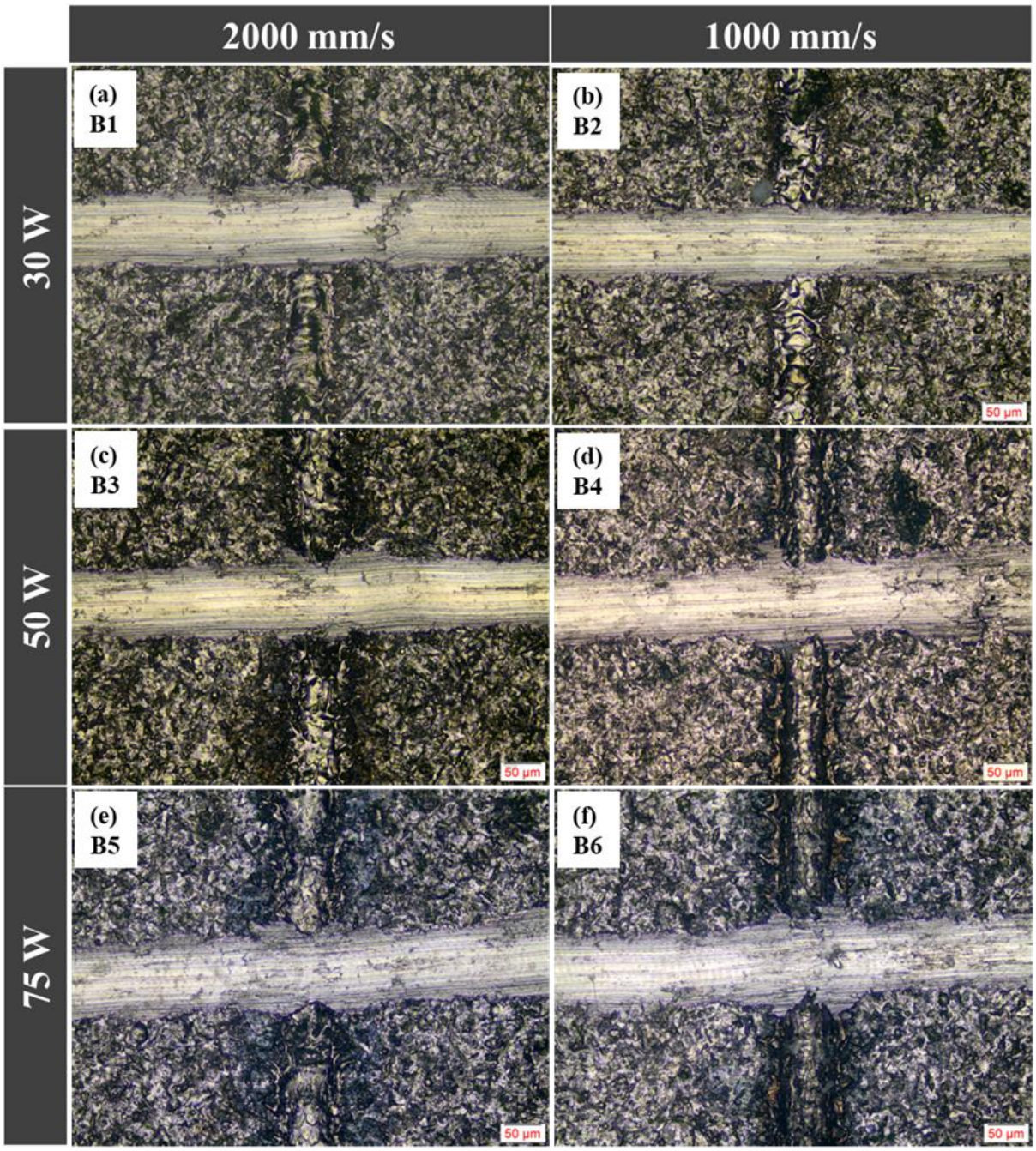

Figure 22. LM images showing the scratched surfaces of laser treated NiAl alloy under argon condition obtained after scratch tests under 15N load.

Figure 23a shows the scratch track obtained in the situation of 30 W laser power and 2000 mm/s scanning speed in the air environment. Under these conditions, the scratch width is 171 µm, while the depth is 7.02 µm. The relatively low pulse energy of 0.6 mJ and influence energy of 305 J/m^2 produces slight thermal accumulation, with small surface alteration. The high scanning speed reduces the interaction time between the laser and the material, preventing excessive heat diffusion and producing a shallow, uniform scratch profile. The surface is quite smooth, which indicates moderate scratch resistance with a hardness-plasticity balance. Figure 23b is the

scratch profile for the same 30 W laser power but at the lower 1000 mm/s scanning speed. The scratch width is narrowed to 101 µm, and the depth is 5.13 µm. Slower scanning speed increases the dwell time, encouraging thermal diffusion and more severe surface restructuring. Compared with Figure 23a, the affected area has greater densification, making the scratch profile slightly deeper but with better wear resistance. The narrower track shows that the surface had developed a higher resistance to plastic deformation due to microstructural changes in the remelted layer.

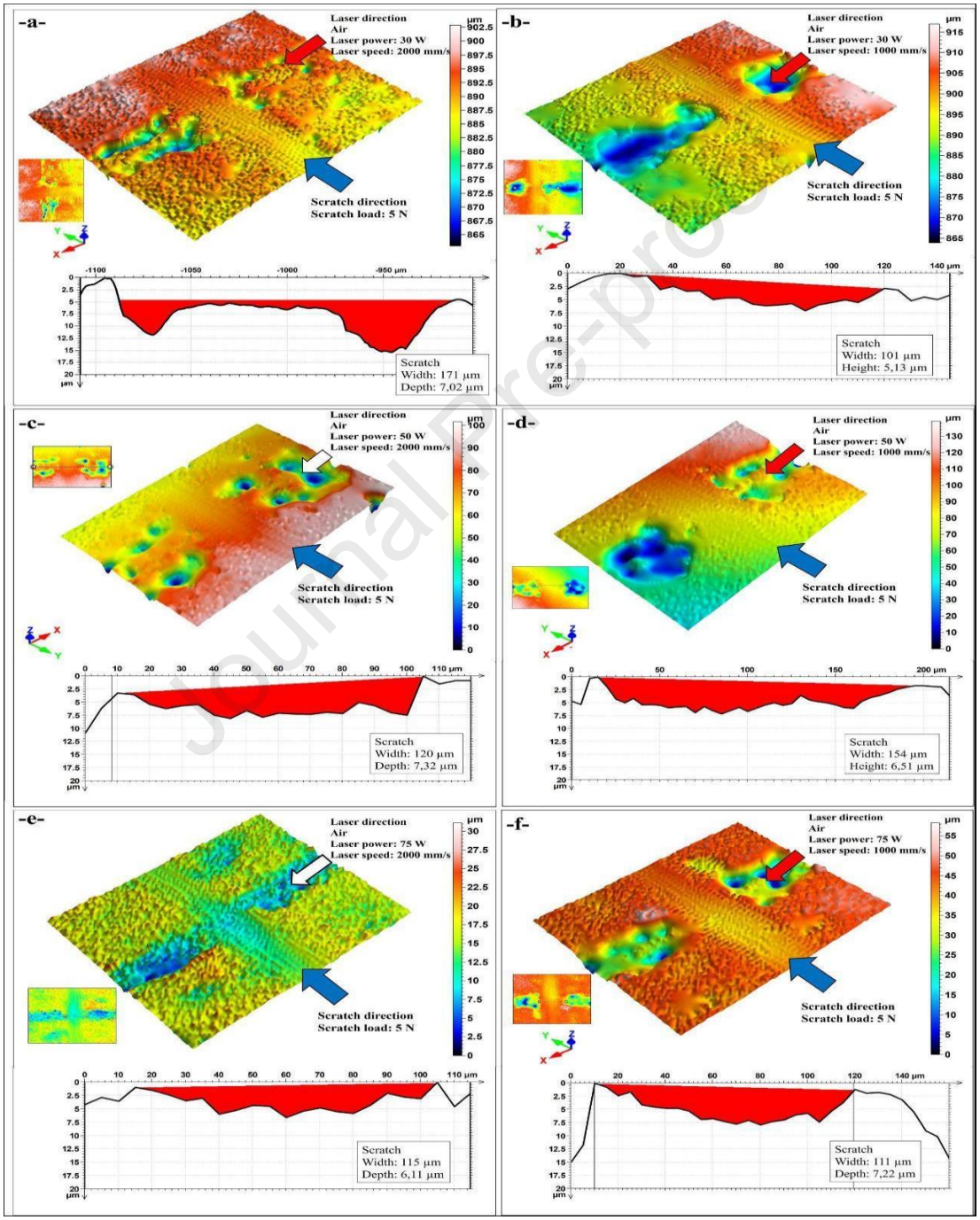

Figure 23. Scratch track (5N load) 3D and cross-sectional profilometer images of laser treated spark plasma sintered nickel aluminide alloy (a) A1, (b) A2, (c) A3, (d) A4, (e) A5, (f) A6.

Figure 23c shows the scratch track when the laser power is 50 W and the scanning speed is 2000 mm/s. Under these conditions, the scratch width is 120 μm, whereas its depth is 7.32 μm. The higher pulse energy of 1.0 mJ and influence energy of 510 J/m^2 result in higher thermal input, leading to more remelting and surface modification. At these conditions relative to the previous ones, the scratch track becomes wider and relatively deeper, which means that the material hardness and toughness are influenced. The consequent increase in scratch resistance is most probably due to the increased phase transformations in the remelted zone, which reinforces the mechanical property of the surface. Figure 23d illustrates the effect of reducing the scanning speed to 1000 mm/s at a laser power of 50 W. The scratch width is considerably larger at 154 μm, but the depth remains 6.51 μm. The longer interaction time between the laser and the material results in longer heat diffusion, which widens the heat-affected zone. The increased width of scratch track proves that the remelted layer is harder to indent, and the decreased but not significantly reduced depth proves that the material is not short of sufficient plasticity to produce brittle fracture. The increased power of the laser and reduced scanning speed in combination generate a well-developed remelted zone with a combination of hardness and toughness. Figure 23e illustrates the scratch behavior under the condition of 75 W laser power and 2000 mm/s scanning speed. The scratch width is 115 μm with a depth of 6.11 μm. The high maximum pulse energy of 1.5 mJ and influence energy of 765 J/m^2 deliver high thermal input, causing intense remelting and densification of the surface. The high scanning speed, however, limits excess accumulation of heat, which precludes over-expansion of the area of remelt. The resultant scratch profile has an optimized surface hardness because depth is preserved in spite of higher thermal energy. The increased surface integrity is favorable to improvement in tribological performance, and this condition is favorable for application where there is structural integrity and wear resistance required. Figure 23f shows the scratch track obtained for 75 W laser power at the lower scan speed of 1000 mm/s. The scratch width is 111 μm, and the depth is 7.22 μm. The high laser power and low scan speed give longer heat exposure, promoting deeper remelting and densification of the material. The comparatively deeper scratch profile indicates a harder surface, and the lower width indicates load-bearing capacity enhancement. The improved thermal effects account for a refined microstructure, improving wear resistance without sacrificing enough plasticity for resisting mechanical stress. The comparison of laser parameters in the air atmosphere reveals distinct trends on scratch behavior. The increased laser power raises the thermal input, causing more phase transformations to improve the surface hardness and wear resistance. The reduced scanning speed extends the dwell time, enabling more heat diffusion in depth and forming the well-

structured remelted zone. The high scanning speed and medium laser power combine to balance hardness and plasticity to achieve the optimal tribological properties. The high power and low scanning speed, which results in high thermal input, can add increased brittleness to the material, which can impact material resistance to mechanical stresses.

The scratch trace for scanning speed of 2000 mm/s and power of 30 W in argon is demonstrated in Figure 24a. The width of the scratch is 105 µm, while depth is 7.60 µm. The low pulse energy of 0.6 mJ and influence energy of 305 J/m^2 creates limited thermal effect in material, minimizing surface modification and oxidation. The high scanning speed restricts accumulation of heat, and there is a smoother surface structure. The argon-shielded specimen, compared to its counterpart produced in air, has smaller width and increased depth of scratch, which is an indication of increased surface hardness due to less oxidation and phase control. The scratch trace in Figure 24b is for the same power of 30 W but for reduced scanning speed of 1000 mm/s. The width of the scratch is decreased to 93 µm, while depth is increased to 9.41 µm. The reduced scanning speed increases dwell time, which leads to increased diffusion of heat, and there is increased remelting effect. The increased depth is an indication of increased surface hardness, while decreased width is an indication of increased load-carrying capacity due to increased microstructural refinement in remelted areas. The scratch trace in Figure 24c is for increased power of 50 W and scanning speed of 2000 mm/s in argon. The width of the scratch is 123 µm, while depth is 15.7 µm. The increased pulse energy of 1.0 mJ and influence energy of 510 J/m^2 increases heat input, which leads to increased depth of remelting and finer microstructure. The higher depth corresponds to higher hardening effect, and the wider scratch profile is an indication of higher wear resistance. Compared to air-processing samples, argon atmosphere results in higher homogeneity of the surface and higher scratch resistance due to suppressed oxidation. The scratches behavior for laser power of 50 W and scanning speed of 1000 mm/s in argon atmosphere is shown in Figure 24d. The depth is 9.31 µm, and width is 92 µm. The higher dwell time increases diffusion of heat, and this increases density and hardness of the remelted zone. The reduced width of scratches is an indication of higher load-carrying capacity, while average depth is an indication of proper hardness and plasticity. The argon atmosphere preserves phase homogeneity, suppresses excess oxidation, and enhances tribological performance. The scratch profile for scanning speed of 2000 mm/s and laser power of 75 W in argon atmosphere is shown in Figure 24e. The depth is 9.21 µm, while width is 132 µm. The maximum pulse energy of 1.5 mJ and influence energy of 765 J/m^2 provides high thermal input, and this leads to high remelting and densification. The high scanning speed,

however, limits excess accumulation of heat, and this leads to controlled surface transformation. The higher width of scratches and average depth indicate higher mechanical stress resistance while ensuring proper plasticity. The scratch track in Figure 24f is developed using reduced scanning speed of 1000 mm/s and 75 W of laser power in argon atmosphere. The depth is increased to 12.46 µm, and width is reduced to 46 µm. The low scanning speed and high power of the laser generate higher heat input for longer times, and this results in increased material densification and remelting. The much lower width of scratch reveals increased load-carrying capacity, and increased depth reveals increased hardness. The argon shielding inhibits oxidation effectively, and this leads to finer microstructure and enhanced mechanical properties.

In Figure 25a, under the laser conditions with a power of 30 W and a scan velocity of 2000 mm/s in the air ambient atmosphere, a scratch track with a width of 102 µm and depth of 9.06 µm was determined. The low pulse energy 0.6 mJ and influence energy 305 J/m^2 caused insignificant modifications on the surface, because high scanning speed restricts thermal accumulation. These conditions produced a shallow scratch profile with moderate width, consistent with the lower thermal input. Decreased in Figure 25b under the same air atmosphere (laser power was held the same to 30 W), after scanning speed reaches the levels of only 1000 mm/s, the depth increases against 9.92 µm, in Figure 25b and while the track was reduced from 65 µm. Enhanced dwell time results in deep heat diffusion enhancement and shifting of morphological features appearing on the treated surface toward narrower yet more profound scratch profiles, by comparison in Figure 25a, evidence for much more localized absorption energy under operating conditions shown here. In Figure 25c, scratch track width increased to 110 µm with 7.28 µm in depth, under the laser power of 50 W and scanning speed of 2000 mm/s in the air atmosphere. The larger pulse energy of 1 mJ and influence energy of 510 J/m^2 resulted in a stronger thermal impact, hence broader and shallower scratch profile. This means, with increased power of the laser, this result infers a more enormous input of energy per unit area, though the depth was limited by the high scanning speed. In Figure 25d, in an air atmosphere, for a laser power of 50 W and a scanning speed of 1000 mm/s, the scratch track width significantly widened to 138 µm with a depth of 9.66 µm. Higher power coupled with reduced scanning speed increased the dwell time and heat input and thus resulted in increased surface modification. The broad and deep scratch profile indicated substantial thermal and mechanical effects on the material surface.

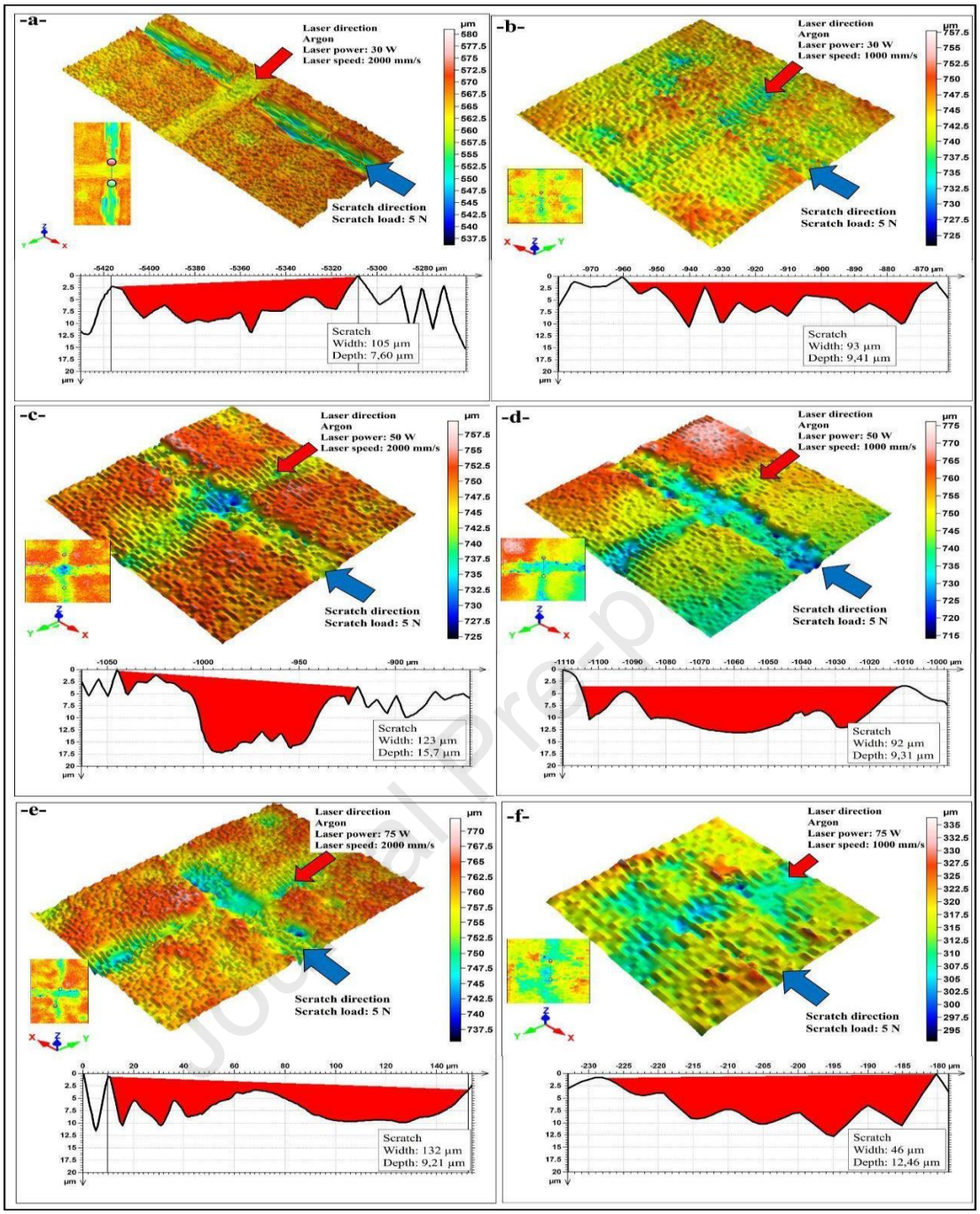

Figure 24. Scratch track (5N load) 3D and cross-sectional profilometer images of laser treated spark plasma sintered nickel aluminide alloy (a) B1, (b) B2, (c) B3, (d) B4, (e) B5, (f) B6.

In Figure 25e, at a laser power of 75 W and a scanning speed of 2000 mm/s in an air atmosphere, the scratch track width reduced to 106 µm, whereas the depth increased to 12.94 µm. The pulse energy of 1.5 mJ and influence energy of 765 J/m^2 provided high thermal input, but the high scanning speed moderated the extent of surface modification. This increase in depth relative to width would suggest that the energy was concentrated in a small area while processing.

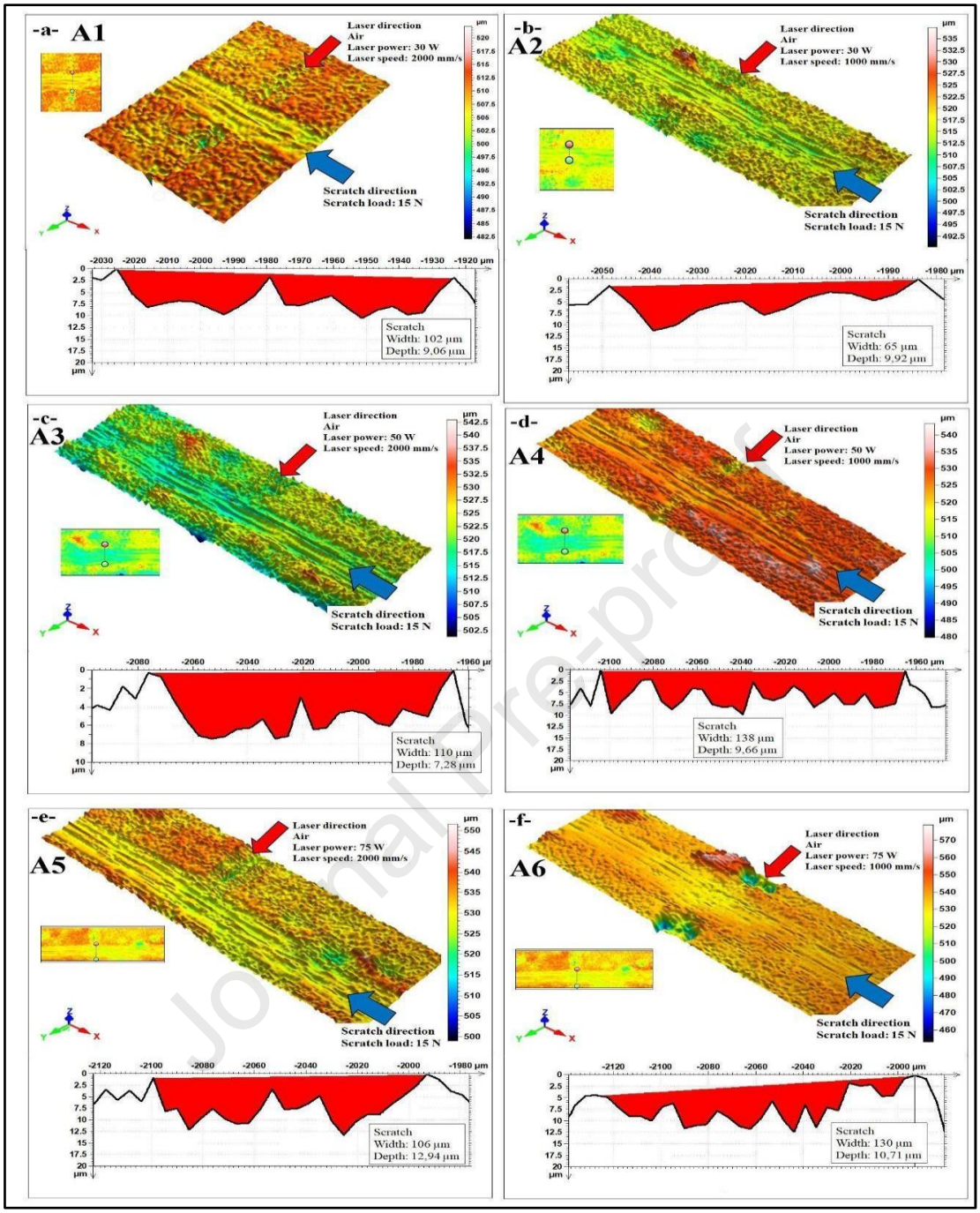

Figure 25. Scratch track (15N load) 3D and cross-sectional profilometer images of laser treated spark plasma sintered nickel aluminide alloy (a) A1, (b) A2, (c) A3, (d) A4, (e) A5, (f) A6.

In Figure 25f, scratch track width increased to 130 µm with a depth of 10.71 µm for the application of 75 W laser power at scanning speed 1000 mm/s in the air atmosphere. Reduced scanning speed along with high laser power maximized the thermal input causing intensive surface modification. A broad and deep scratch profile indicates joint effects of high energy with longer dwell time on the material surface. The trend and variations of the rough result presented indicate that both scanning speed and laser power serve as two most controlling

parameters during determination of scratch morphology, keeping in air atmosphere: at larger value, scratch track obtained for higher power becomes increasingly broader and deeper because enhanced laser energy increases the role of a thermal effect, which decreases in case of faster modification by the moving scan field, as this places restrictions for development of its maximum impact. This indicates a perfect balance of the operating variables during laser processing that aims for certain characteristics at surfaces.

It should be seen in Figure 26a, when the laser power and the scanning speed is at 30 W and 2000 mm/s under argon atmosphere condition, it shows the scratch track is 112 µm with a depth of 7.79 µm, whereas relatively small scratches are attributed to very small pulse energy value of 0.6 mJ with its consequence of very small value for influence energy which amounted to only 305 J/m^2 while heating affected processes would become minimal in this range for an inert ambient surrounding (argon). The shielding effect from the argon ensured that there was a decrease in surface oxidation, hence heat dissipation was controlled, leading to a more regular morphology. Figure 26b, still at 30 W laser power in argon, but with a 1000 mm/s scanning speed-a scratch track width and depths reached 132 µm and 10.99 µm separately. A slower scan rate means increased dwell time through lengthening of the energy absorption effect, producing expansion in the thermal field influence that leads to a deeper fabrication. Argon provides shallow heat treatment that may cause any oxidation during the process. The increase in these phenomena, though, further enhanced localized thermal effects. Figure 26c: With the increase in laser power to 50 W and a scanning velocity of 2000 mm/s in the argon atmosphere, the scratch track width reduced to 98 µm with a depth of 7.47 µm. Higher laser power increased the pulse energy up to 1 mJ and influenced energy up to 510 J/m^2; however, high scanning speed limited the heat accumulation. The resulting scratch is narrower and shallower, reflecting controlled heat diffusion in the presence of argon shielding. The scratch track width was significantly narrowed to 65 µm, and the depth decreased to 5.32 µm when the laser power and scanning speed were set to 50 W and 1000 mm/s, respectively, in an argon atmosphere in Figure 26d. As the scanning speed slowed down, it led to more energy absorption. Yet again, the heat diffusion and surface oxidation were controlled under this protective argon environment. Hence, this condition obtained a notably reduced scratch profile when compared to air atmosphere for similar parameters (Figure 26e). The scratch track is 60 µm wide, 6.1 µm deep for the input parameters: laser power (75 W) and scanning speed (2000 mm/s) in argon shielding. Although a pulse energy of 1.5 mJ is an influencing energy of 765 J/m^2 that exerts considerable thermal input, due to high scanning speed, coupled with the presence of argon

shielding, the extent of modification of the surface was contained to this value. The shallow profile reflects the moderating influence of high speed and inert atmosphere under elevated power conditions.

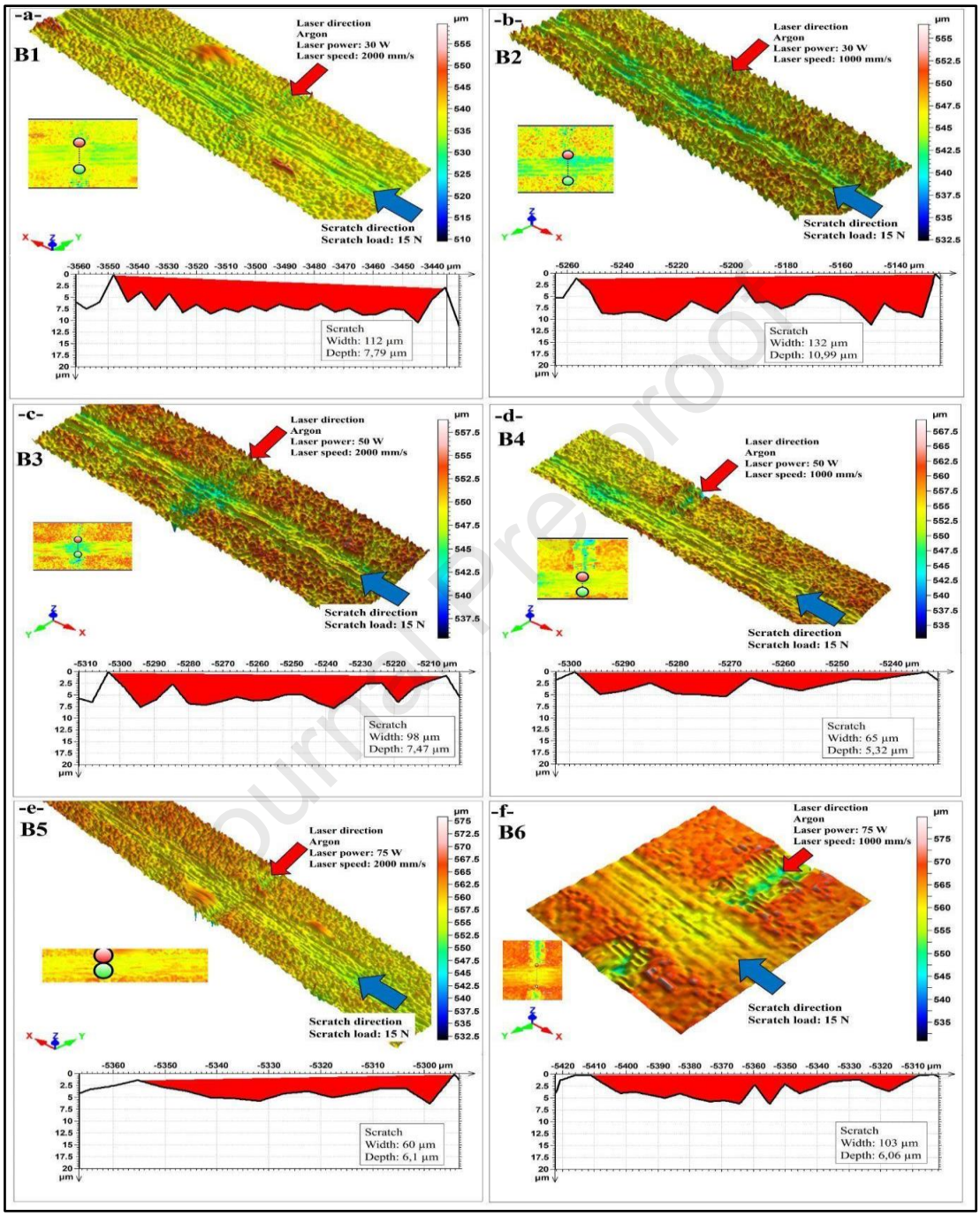

Figure 26. Scratch track (15N load) 3D and cross-sectional profilometer images of laser treated spark plasma sintered nickel aluminide alloy (a) B1, (b) B2, (c) B3, (d) B4, (e) B5, (f) B6.

In Figure 26f, scratch track width increased to 103 µm with a depth of 6.06 µm under laser power of 75 W and scanning speed of 1000 mm/s in an argon atmosphere. The slower scanning speed increased the thermal input, hence increasing the energy transferred to the surface.

However, the argon atmosphere effectively controlled heat dissipation and prevented too serious surface damage. The scratch profile in such a case reflects the balance of thermal effects in the high-power condition within the inert environment. These observations also point out that the argon atmosphere plays a considerable role in the regulation of oxidation and thermal diffusion during laser processing. Indeed, slower scanning speed with higher laser power results in greater thermal impact but provides almost similar surface structure because of the inert shielding. Thus, the interaction between the parameters also is manifested in scratch morphology as Ar shielding resulted in much finer profiles compared to their air-processed counterparts.

4. Conclusion

The microstructure and scratch resistance of nickel aluminide (NiAl) alloys sintered through spark plasma sintering can be enhanced significantly through laser-induced remelting, which alters their microstructure and mechanical properties. The research demonstrated that the remelting zones underwent severe phase transformations, primarily due to aluminum depletion, which altered the phase balance of NiAl and Ni_3Al. Thermodynamic simulation and experiment demonstrated that modified zones in the remelted zones comprised finer microstructure and eutectic Ni_3Al-NiAl phases, which contributed to enhanced wear resistance. The extent of aluminum evaporation and redistribution was increased in increased powers and decreased scanning velocities, which contributed to increased hardness in modified zones.

The microstructure and dimension of the remelted and heat-affected zones varied significantly under different laser processing and atmospheric conditions. In air, microstructure changes were caused by oxidation, which increased the prevalence of oxide-rich zones and impacted mechanical properties. In argon shielding, oxidation was suppressed, and this produced homogenized microstructure and increased phase stability. The width of the heat affected zone was 60 µm to 131 µm in air but was reduced to 58 µm to 109 µm in argon. The state of oxidation directly affected surface hardness and wear resistance, and argon-treated samples exhibited better tribological properties due to decreased defects due to oxidation.

Scratch tests demonstrated that increased surface hardness and plastic deformation resistance resulted from laser-induced remelting. Under 5N applied loads, untreated samples exhibited wear depths of more than 9 µm, while laser-treated surfaces, particularly those treated using 75 W and 2000 mm/s in argon, exhibited a reduction in depth of scratches of about 40% to around 5.4 µm. At higher applied loads of 15N, there was increased material loss in untreated surfaces,

where maximum depths of scratches of 12.9 μm were recorded. The argon-treated samples, in contrast, demonstrated reduced depth of 10.9 μm, which indicated their enhanced hardness and mechanical stress resistance. Lower scanning speed further increased wear resistance and enhanced depth of remelting and material density, which was evidenced in narrower and deeper scratch tracks.

The tribological performance of the remelted surfaces was influenced by atmospheric conditions and laser power. Microcrack initiation in the interface of the heat affected zone and matrix was seen in air-treated samples, suggesting that defects produced by oxidation acted as stress concentrators under high loads. The argon-treated surfaces, in contrast, exhibited decreased brittle fracture, which indicated enhanced ductility and mechanical integrity. The high-energy treatment with a laser was also shown to enhance the integrity of the surface while attaining proper combination of hardness and plasticity, which is critical in wear-resistant applications.

Whereas the single-pass process made possible a simple assessment of the effects of remelting, laser remelting in multi-pass better mimics conditions in practical processing of larger surface areas. Repeated thermal exposure and overlapping tracks in multi-pass approaches might produce specific microstructural characteristics—grain size heterogeneities, phase redistribution, and residual stress—that have a strong impact on scratch resistance. Controlled multi-pass remelting will therefore be the focus of subsequent work to determine surface evolution and tribology under accumulative heating and to validate the scalability of the observed enhancements. The possibility of modulating the microstructure and mechanical behavior of NiAl alloys through laser-induced remelting is of high interest for high-temperature applications, including aerospace, energy, and wear-resistant coating. The results show that argon-assisted treatment is to be recommended for oxidation and enhanced durability in demanding situations, and that air treatment can prove to be satisfactory in cost-based conditions where mild oxidation is acceptable. The results show that laser surface treatment is an accurate and effective method of optimizing intermetallic alloys' tribological performance. The future research should target to extend tribological tests to sliding and reciprocating conditions, investigate the long-term thermal stability of laser-treated surfaces, and investigate hybrid approaches combining laser remelting and subsequent treatment techniques such as laser shock peening or ion implantation. The work demonstrates that laser-induced remelting is indeed a potential method to enhance the surface properties of NiAl-based alloys and provides valuable guidelines to their application in harsh conditions.

Journal Pre-proof

Acknowledgements

This work was supported by the Kocaeli University Scientific Research Projects Coordination Unit [Project No: FBA-2024-4297].

References

[1] M.A. Awotunde, A.O. Adegbenjo, O.O. Ayodele, A.M. Okoro, M.B. Shongwe, P.A. Olubambi, Reactive synthesis of CNTs reinforced nickel aluminide composites by spark plasma sintering, Mater. Sci. Eng. A 796 (2020) 140070, https://doi.org/10.1016/j.msea.2020.140070.

[2] M. Awotunde, A. Adegbenjo, O. Ayodele, M. Okoro, M. Shongwe, P. Olubambi, Effects of carbon nanotube weight fraction on the fracture toughness of spark plasma sintered nickel aluminide-$NiAl_3$, Mater. Today Proc. 28 (2) (2020) 625–629, https://doi.org/10.1016/j.matpr.2019.12.233.

[3] M. Abedi, K. Kuskov, D. Moskovskikh, E.V. Zakharova, D. Belov, A. Mukasyan, Reactive spark plasma sintering of NiAl intermetallics: A comparative study, Intermetallics 152 (2023) 107750, https://doi.org/10.1016/j.intermet.2022.107750.

[4] Z. Zhao, C. Wang, L. Yang, Y. Cheng, Z. Cai, M.Z. Mehrizi, Microstructure and properties of NiAl/TiC composite synthesized by spark plasma sintering of mechanically activated elemental powders, Ceram. Int. 49 (10) (2023) 15710–15716, https://doi.org/10.1016/j.ceramint.2023.01.163.

[5] D.V. Dudina, A.K. Mukherjee, Reactive spark plasma sintering: successes and challenges of nanomaterial synthesis, J. Nanomater. 2013 (2013) 625218, https://doi.org/10.1155/2013/625218.

[6] K. Morsi, Combustion synthesis and the electric field: a review, Int. J. Self-Propag. High-Temp. Synth. 26 (3) (2017) 199–209, https://doi.org/10.3103/S1061386217030037.

[7] A.S. Mukasyan, A.S. Rogachev, D.O. Moskovskikh, Z.S. Yermekova, Reactive spark plasma sintering of exothermic systems: a critical review, Ceram. Int. 48 (3) (2022) 2988–2998, https://doi.org/10.1016/j.ceramint.2021.10.207.

[8] S.S. Dong, P. Hou, H.Y. Cheng, H.B. Yang, G.T. Zou, Fabrication of intermetallic NiAl by self-propagating high-temperature synthesis reaction using aluminium nanopowder under high

pressure, J. Phys. Condens. Matter 14 (44) (2002) 11023–11030, https://doi.org/10.1088/0953-8984/14/44/421.

[9] M. Awotunde, P. Olubambi, D. Chen, Influence of process parameters on the sintering behaviour and densification of NiAl intermetallics fabricated by spark plasma sintering, Mater. Today Proc. 38 (2) (2021) 1159–1163, https://doi.org/10.1016/j.matpr.2020.07.142.

[10] L.I. Shevtsova, M.A. Korchagin, M.A.V.S. Lozhkin, A.I. Gavrilov, A.Y. Larichkin, Structure and properties of an Ni_3Al intermetallic compound formed as a result of spark plasma sintering of the powder mixtures prepared by various methods, Metallurgist 65 (2022), https://doi.org/10.1007/s11015-022-01273-7.

[11] P.J. Blau, C.E. DeVore, Sliding friction and wear behaviour of several nickel aluminide alloys under dry and lubricated conditions, Tribol. Int. 23 (4) (1990) 226–234, https://doi.org/10.1016/0301-679X(90)90027-M.

[12] K. Ganesh Kumar, Sivarao, T.J.S. Anand, A novel intermetallic nickel aluminide (Ni_3Al) as an alternative automotive body material, Int. J. Eng. Technol. IJET-IJENS 11 (1) (2011) 208–215.

[13] O.O. Ayodele, M.A. Awotunde, M.B. Shongwe, A.O. Adegbenjo, B.J. Babalola, B.J. Obadele, et al., Effect of heating rate on the microstructure and mechanical properties of spark plasma sintered CNTs reinforced nickel aluminide, Key Eng. Mater. 821 (2019) 440–444, https://doi.org/10.4028/www.scientific.net/kem.821.440.

[14] A. Mohammadnejad, A. Bahrami, M. Sajadi, P. Karimi, H.R. Fozveh, M. Yazdan Mehr, Microstructure and mechanical properties of spark plasma sintered nanocrystalline Ni_3Al-xB ($0.0<x<1.5$ at%) alloy, Mater. Today Commun. 17 (2018) 161–168, https://doi.org/10.1016/j.mtcomm.2018.09.002.

[15] J. Wu, J. Yu, W. Wang, S. Gao, J. Luo, C. Li, Z. Ma, Y. Liu, Influences of laser remelting treatments on microstructure and tensile properties of multiphase Ni_3Al-based intermetallic alloy, Mater. Sci. Eng. A 857 (2022) 144087, https://doi.org/10.1016/j.msea.2022.144087.

[16] S. Akhtar, N. Akhtar, I. Nadeem, A. Tauqir, Rapid solidification and surfaces alloying using continuous CO_2 laser to generate Ni-aluminide on steel, Key Eng. Mater. 875 (2021) 329–336, https://doi.org/10.4028/www.scientific.net/kem.875.329.

Journal Pre-proof

[17] K.V. Ivanov, K.O. Akimov, E.K. Ivanova, M.G. Figurko, Microstructure and properties of Ni_3Al-TiC surface composites formed on Ni_3Al using low-energy high-current electron beam, Vacuum 230 (2024) 113606, https://doi.org/10.1016/j.vacuum.2024.113606.

[18] S. Han, X. Lei, W. Xia, J. Guo, R. Yang, J. Liu, W. Yao, N. Wang, Optimizing the electrochemical corrosion performance of laser cladded Ni-based single crystal superalloy via manipulation of γ′(Ni_3Al) phase, Surf. Coat. Technol. 467 (2023) 129700, https://doi.org/10.1016/j.surfcoat.2023.129700.

[19] Y. Cai, Z. Dong, L. Zhao, Y. Peng, Y. Cao, The effect of laser power on the microstructure and wear resistance of a Ni_3Al-based alloy cladding layer deposited via laser cladding, Coatings 14 (2024) 317, https://doi.org/10.3390/coatings14030317.

[20] M. Zhang, Y. Wang, Z. Ma, Z. Wang, Z. Yang, Non-uniform high-temperature oxidation behavior of twin wire and arc additive manufactured Ni_3Al-based alloy, J. Manuf. Process. 84 (2022) 522–530, https://doi.org/10.1016/j.jmapro.2022.10.035.

[21] G. Lu, W. Lu, X. Shi, W. Zhai, J. Zhang, Z. Yang, W. Chen, Tribological properties and self-compensating lubrication mechanisms of Ni_3Al matrix bio-inspired shell-like composite structure, Appl. Surf. Sci. 573 (2022) 151462, https://doi.org/10.1016/j.apsusc.2021.151462.

[22] Z. Liu, F. Yin, C. Chen, L. Zhao, L. Fu, Y. Feng, Y. Cao, Y. Peng, Z. Tian, C. Li, Microstructure and wear resistance of a Cr_7C_3 reinforced Ni_3Al composite coating prepared by laser cladding, Coatings 12 (2022) 105, https://doi.org/10.3390/coatings12010105.

[23] F. Li, C. Zhang, Y. Li, Q. Pang, Effects of laser remelting on frictional properties of supersonic flame-sprayed coatings, Coatings 14 (2024) 325, https://doi.org/10.3390/coatings14030325.

[24] N. Akhtar, M. Afzal, R. Akhter, Microstructure and wear properties of laser treated Ni_3Al coatings on low alloy medium carbon steel, Lasers Manuf. Mater. Process. 5 (2018) 283–297, https://doi.org/10.1007/s40516-018-0065-3.

[25] Y. Song, G. He, Y. Wang, Y. Chen, Tribological behavior of boron nitride nanoplatelet reinforced Ni_3Al intermetallic matrix composite fabricated by selective laser melting, Mater. Des. 165 (2019) 107579, https://doi.org/10.1016/j.matdes.2018.107579.

[26] I. Zhirnov, D.V. Kotoban, A.V. Gusarov, Evaporation-induced gas-phase flows at selective laser melting, Appl. Phys. A 124 (2018) 157, https://doi.org/10.1007/s00339-017-1532-y.

[27] D. Zhang, P. Zhang, Z. Liu, Z. Feng, C. Wang, Y. Guo, Thermofluid field of molten pool and its effects during selective laser melting (SLM) of Inconel 718 alloy, Addit. Manuf. 21 (2018) 567–578, https://doi.org/10.1016/j.addma.2018.03.031.

[28] P. Tang, H. Xie, S. Wang, et al., Numerical analysis of molten pool behavior and spatter formation with evaporation during selective laser melting of 316L stainless steel, Metall. Mater. Trans. B 50 (2019) 2273–2283, https://doi.org/10.1007/s11663-019-01641-w.

[29] W. Zhang, Y. Peng, Z. Liu, Molecular dynamics simulations of the melting curve of NiAl alloy under pressure, AIP Adv. 4 (5) (2014) 057110, https://doi.org/10.1063/1.4876515.

[30] M.W. Brumm, H.J. Grabke, Oxidation behaviour of NiAl—II. Cavity formation beneath the oxide scale on NiAl of different stoichiometries, Corros. Sci. 34 (4) (1993) 547–561, https://doi.org/10.1016/0010-938X(93)90271-H.

[31] H. Li, A. Hesnawi, X. Fan, S. Gong, H. Xu, Inter-diffusion and oxidation behavior in electron-beam evaporated NiAl coatings, Vacuum 81 (3) (2006) 329–337, https://doi.org/10.1016/j.vacuum.2006.05.010.

[32] O. Hunziker, W. Kurz, Solidification microstructure maps in NiAl alloys, Acta Mater. 45 (12) (1997) 4981–4992, https://doi.org/10.1016/S1359-6454(97)00194-8.

[33] A. Pasturel, C. Colinet, A.T. Paxton, M. van Schilfgaarde, First-principles determination of the Ni-Al phase diagram, J. Phys. Condens. Matter 4 (4) (1992) 945, https://doi.org/10.1088/0953-8984/4/4/005.

[34] W. Shao, J.M. Guevara-Vela, A. Fernández-Caballero, S. Liu, J. LLorca, Accurate prediction of the solid-state region of the Ni-Al phase diagram including configurational and vibrational entropy and magnetic effects, Acta Mater. 253 (2023) 118962, https://doi.org/10.1016/j.actamat.2023.118962.

[35] L.I. Shevtsova, M.A. Korchagin, A. Thömmes, V.I. Mali, A.G. Anisimov, S.Y. Nagavkin, Spark plasma sintering of mechanically activated Ni and Al powders, Adv. Mater. Res. 1040 (2014) 772–777.

Journal Pre-proof

[36] I.A. Ditenberg, D.A. Osipov, I.V. Smirnov, K.V. Grinyaev, Thermal stability of Ni_3Al microstructure and microhardness after spark plasma sintering, Intermetallics 164 (2024) 108105, https://doi.org/10.1016/j.intermet.2023.108105.

[37] O.O. Ayodele, A.O. Adegbenjo, M.A. Awotunde, M.B. Shongwe, P.A. Olubambi, The influence of heating rate on the microstructural evolutions and mechanical properties of spark plasma sintered multi-walled carbon nanotubes reinforced NiAl intermetallic matrix composites, Mater. Sci. Eng. A 773 (2020) 138869, https://doi.org/10.1016/j.msea.2019.138869.

[38] M.A. Awotunde, O.O. Ayodele, A.O. Adegbenjo, et al., NiAl intermetallic composites—a review of processing methods, reinforcements and mechanical properties, Int. J. Adv. Manuf. Technol. 104 (2019) 1733–1747, https://doi.org/10.1007/s00170-019-03984-9.

[39] P. Hyjek, M. Stępień, R. Kowalik, I. Sulima, Corrosion resistance of nickel-aluminum sinters produced by high-pressure HPHT/SPS method, Mater. 16 (5) (2023) 1907, https://doi.org/10.3390/ma16051907.

[40] P. Bhagtani, Modelling Thermal Conductivity of Al-Fe, Al-Ni, and Al-Co Spark Plasma Sintered (SPS) Alloys. Master of Applied Science in Engineering Thesis, The University of Guelph, Guelph, Ontario, Canada, 2020.

[41] J. Cinert, Study of Mechanisms of the Spark Plasma Sintering Technique. Doctoral Thesis, Czech Technical University in Prague, Faculty of Electrical Engineering, Department of Electrotechnology, Prague, Czech Republic, 2018.

[42] Y. Li, M. Založnik, J. Zollinger, L. Dembinski, A. Mathieu, Effects of the powder, laser parameters and surface conditions on the molten pool formation in the selective laser melting of IN718, J. Mater. Process. Technol. 289 (2021) 116930, https://doi.org/10.1016/j.jmatprotec.2020.116930.

[43] A. Temmler, W. Dai, T. Schmickler, M.E. Küpper, C.L. Häfner, Experimental investigation on surface structuring by laser remelting (WaveShape) on Inconel 718 using varying laser beam diameters and scan speeds, Appl. Surf. Sci. 541 (2021) 147814, https://doi.org/10.1016/j.apsusc.2020.147814.

Journal Pre-proof

[44] L. Wang, J. Yao, Y. Hu, S. Song, Suppression effect of a steady magnetic field on molten pool during laser remelting, Appl. Surf. Sci. 351 (2015) 794–802, https://doi.org/10.1016/j.apsusc.2015.05.179.

[45] A. Temmler, E. Willenborg, K. Wissenbach, Design surfaces by laser remelting, Phys. Procedia 12 (A) (2011) 419–430, https://doi.org/10.1016/j.phpro.2011.03.053.

[46] H. Gu, T. Väistö, L. Li, Numerical and experimental study on the molten pool dynamics and fusion zone formation in multi-pass narrow gap laser welding, Opt. Laser Technol. 126 (2020) 106081, https://doi.org/10.1016/j.optlastec.2020.106081.

[47] Z. Guo, L. Wang, C. Wang, X. Ding, J. Liu, Heat transfer, molten pool flow micro-simulation, and experimental research on molybdenum alloys fabricated via selective laser melting, Mater. (Basel) 14 (1) (2020) 75, https://doi.org/10.3390/ma14010075.

[48] A.F. Schon, G.L. de Gouveia, B.S. Sobral, J.E. Spinelli, R. Riva, A.G. Capella, B.L. Silva, Microstructure and hardness of laser remelted surfaces of Al-5%Cu and Al-4%Cu-1%Ni alloys, J. Alloys Compd. 954 (2023) 170189, https://doi.org/10.1016/j.jallcom.2023.170189.

[49] D. Chen, G. Li, P. Wang, Z. Zeng, Y. Tang, Numerical simulation of melt pool size and flow evolution for laser powder bed fusion of powder grade Ti6Al4V, Finite Elem. Anal. Des. 223 (2023) 103971, https://doi.org/10.1016/j.finel.2023.103971.

[50] J. Wang, R. Zhu, Y. Liu, L. Zhang, Understanding melt pool characteristics in laser powder bed fusion: An overview of single- and multi-track melt pools for process optimization, Adv. Powder Mater. 2 (4) (2023) 100137, https://doi.org/10.1016/j.apmate.2023.100137.

[51] Z. Xue, L. Xu, Z. Chen, Y. Sun, L. Zhao, K. Hao, Y. Han, Formation optimization of downward overlaid Inconel 625 on curved surface of X65 pipeline basing on dynamic behavior of molten pool, J. Mater. Res. Technol. 25 (2023) 6356–6368, https://doi.org/10.1016/j.jmrt.2023.07.084.

[52] N. Sobczak, J. Sobczak, R. Asthana, The mystery of molten metal, China Foundry 7 (11) (2010) 425–437.

[53] F.Y. Zhang, K. Mukai, K. Takagi, M. Ohtaka, W.L. Huang, Q.S. Liu, Surface tension and its temperature coefficient of molten tin determined with the sessile drop method at different

Journal Pre-proof

Journal Pre-proof

oxygen partial pressures, J. Colloid Interface Sci. 254 (2) (2002) 338–345, https://doi.org/10.1006/jcis.2002.8589.

[54] W. Liu, J.N. DuPont, Effects of melt-pool geometry on crystal growth and microstructure development in laser surface-melted superalloy single crystals: mathematical modeling of single-crystal growth in a melt pool (part I), Acta Mater. 52 (16) (2004) 4833–4847, https://doi.org/10.1016/j.actamat.2004.06.041.

[55] W. Li, Y. Yang, F. Zhou, Research on formation mechanism of laser cladding micro-melt pool based on multi-model coupling simulation technology, J. Mater. Eng. Perform. (2025), https://doi.org/10.1007/s11665-025-10792-8.

[56] A.F. Mills, Heat Transfer, Second Edition, Prentice-Hall, New Jersey, 1999.

[57] Y. Zhao, Y. Koizumi, K. Aoyagi, D. Wei, K. Yamanaka, A. Chiba, Comprehensive study on mechanisms for grain morphology evolution and texture development in powder bed fusion with electron beam of Co-Cr-Mo alloy, Materialia 6 (2019) 100346, https://doi.org/10.1016/j.mtla.2019.100346.

[58] M. Rettenmayr, Melting and remelting phenomena, Int. Mater. Rev. 54 (1) (2009) 1–17, https://doi.org/10.1179/174328009X392930.

[59] X.X. Wei, X. Lin, W. Xu, Q.S. Huang, M. Ferry, J.F. Li, Y.H. Zhou, Remelting-induced anomalous eutectic formation during solidification of deeply undercooled eutectic alloy melts, Acta Mater. 95 (2015) 44–56, https://doi.org/10.1016/j.actamat.2015.05.014.

[60] X. Wang, S. Kustov, J. Van Humbeeck, A short review on the microstructure, transformation behavior and functional properties of NiTi shape memory alloys fabricated by selective laser melting, Mater. 11 (2018) 1683, https://doi.org/10.3390/ma11091683.

[61] F. Cardarelli, Common Nonferrous Metals, in: Materials Handbook, Springer, London, 2000, https://doi.org/10.1007/978-1-4471-3648-4_2.

[62] S. Chowdhury, N. Yadaiah, C. Prakash, S. Ramakrishna, S. Dixit, L.R. Gupta, D. Buddhi, Laser powder bed fusion: a state-of-the-art review of the technology, materials, properties & defects, and numerical modelling, J. Mater. Res. Technol. 20 (2022) 2109–2172, https://doi.org/10.1016/j.jmrt.2022.07.121.

[63] M.M. Imran, C. Idris, L.C. De Silva, Y.B. Kim, P.E. Abas, Advancements in 3D printing: directed energy deposition techniques, defect analysis, and quality monitoring, Technol. 12 (6) (2024) 86, https://doi.org/10.3390/technologies12060086.

[64] J. Dutta Majumdar, I. Manna, Laser material processing, Int. Mater. Rev. 56 (5–6) (2011) 341–388, https://doi.org/10.1179/1743280411Y.0000000003.

[65] H. Juárez, E. Yousefi, A. Kunwar, Y. Sun, M. Guo, N. Moelans, D. Seveno, Modeling of surface phenomena of liquid Al-Ni alloys using molecular dynamics, Sci. Rep. 13 (1) (2023) 4642, https://doi.org/10.1038/s41598-023-31844-w.

[66] M.S. Raza, S. Datta, K. Vivekanand, et al., Surface modification of high-carbon steel using fiber laser and its thermal, microstructural and tribological analysis, J. Mater. Eng. Perform. 28 (2019) 1873–1883, https://doi.org/10.1007/s11665-019-03943-1.

[67] M.M. Quazi, M.A. Fazal, A.S.M.A. Haseeb, F. Yusof, H.H. Masjuki, A. Arslan, Laser-based surface modifications of aluminum and its alloys, Crit. Rev. Solid State Mater. Sci. 41 (2) (2015) 106–131, https://doi.org/10.1080/10408436.2015.1076716.

[68] X. Tang, Y. Liang, Q. Chen, Deformation mechanisms of interfacial dislocation networks in Ni/Ni_3Al/Ni alloy under different directions based on molecular dynamics simulation, Vacuum 235 (2025) 114144, https://doi.org/10.1016/j.vacuum.2025.114144.

[69] T. Czeppe, S. Wierzbinski, Structure and mechanical properties of NiAl and Ni_3Al-based alloys, Int. J. Mech. Sci. 42 (8) (2000) 1499–1518, https://doi.org/10.1016/S0020-7403(99)00087-9.

[70] A. Moshkovich, I. Lapsker, Y. Feldman, L. Rapoport, Severe plastic deformation of four FCC metals during friction under lubricated conditions, Wear 386–387 (2017) 49–57, https://doi.org/0.1016/j.wear.2017.05.018.

[71] C. Tiwary, V.V. Gunjal, D. Banerjee, K. Chattopadhyaya, Intermetallic eutectic alloys in the Ni-Al-Zr system with attractive high temperature properties, MATEC Web Conf. 14 (2014) 01005, https://doi.org/10.1051/matecconf/20141401005.

Journal Pre-proof

[72] W. Zhai, L. Bai, R. Zhou, X. Fan, G. Kang, Y. Liu, K. Zhou, Recent progress on wear-resistant materials: designs, properties, and applications, Adv. Sci. 8 (2021) 2003739, https://doi.org/10.1002/advs.202003739.

[73] L. Schmidt, K. Schricker, C. Diegel, et al., Effect of partial and global shielding on surface-driven phenomena in keyhole mode laser beam welding, Weld. World 68 (2024) 1353–1374, https://doi.org/10.1007/s40194-023-01627-y.

[74] H. Rojacz, A. Nevosad, M. Varga, On wear mechanisms and microstructural changes in nano-scratches of FCC metals, Wear 526–527 (2023) 204928, https://doi.org/10.1016/j.wear.2023.204928.

[75] J. Gou, K. Chen, M. Le, G. Wang, J. Liu, G. Tan, D. Li, Y. Zhang, A study on the scratch behavior and two-body abrasion wear resistance of TiC-modified E690 steel cladding, Wear (2025) 205923, https://doi.org/10.1016/j.wear.2025.205923.

[76] B. Palacios, S.M.A.K. Mohammed, T. Paul, G. Garino, C. Maribona, S. Langan, A. Agarwal, Scratch-induced deformation behavior of wire-arc directed energy deposited α-Titanium, Mater. 18 (3) (2025) 724, https://doi.org/10.3390/ma18030724.

[77] C. Chen, T. Cao, C. Xie, S. Xu, T. Hu, H. Liao, J. Wang, Z. Ren, Recent progress in laser additive manufacturing of intermetallic alloys: defects, microstructure, and mechanical properties, Addit. Manuf. Front. 4 (2025) 200187, https://doi.org/10.1016/j.amf.2024.200187.

Journal Pre-proof

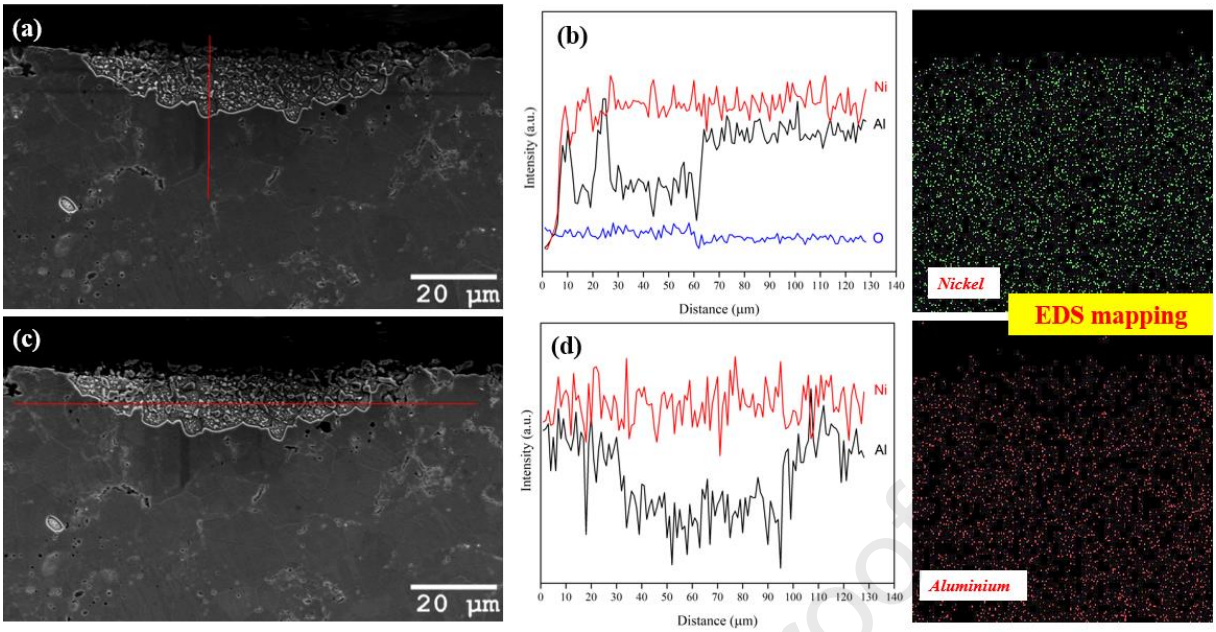

Figure 17. SEM-EDS data of the horizontal (a and b) and the vertical (c and d) EDS line scan of the remelted zone on A1 alloy.

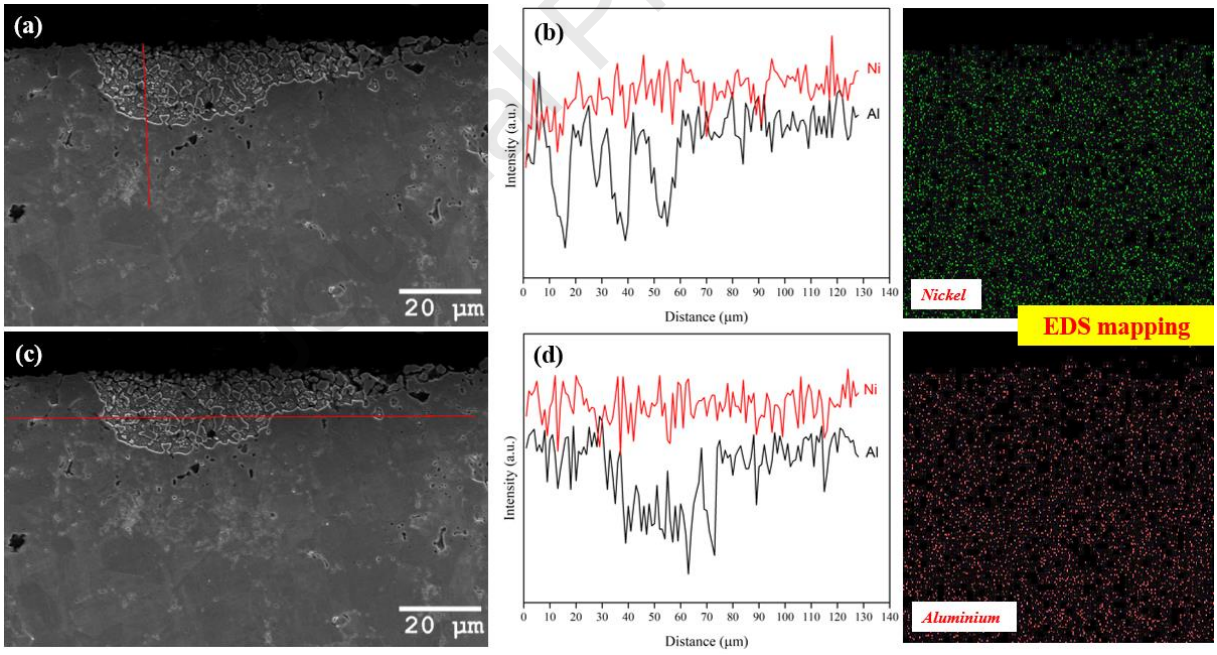

Figure 18. SEM-EDS data of the horizontal (a and b) and the vertical (c and d) EDS line scan of the remelted zone on B1 alloy.

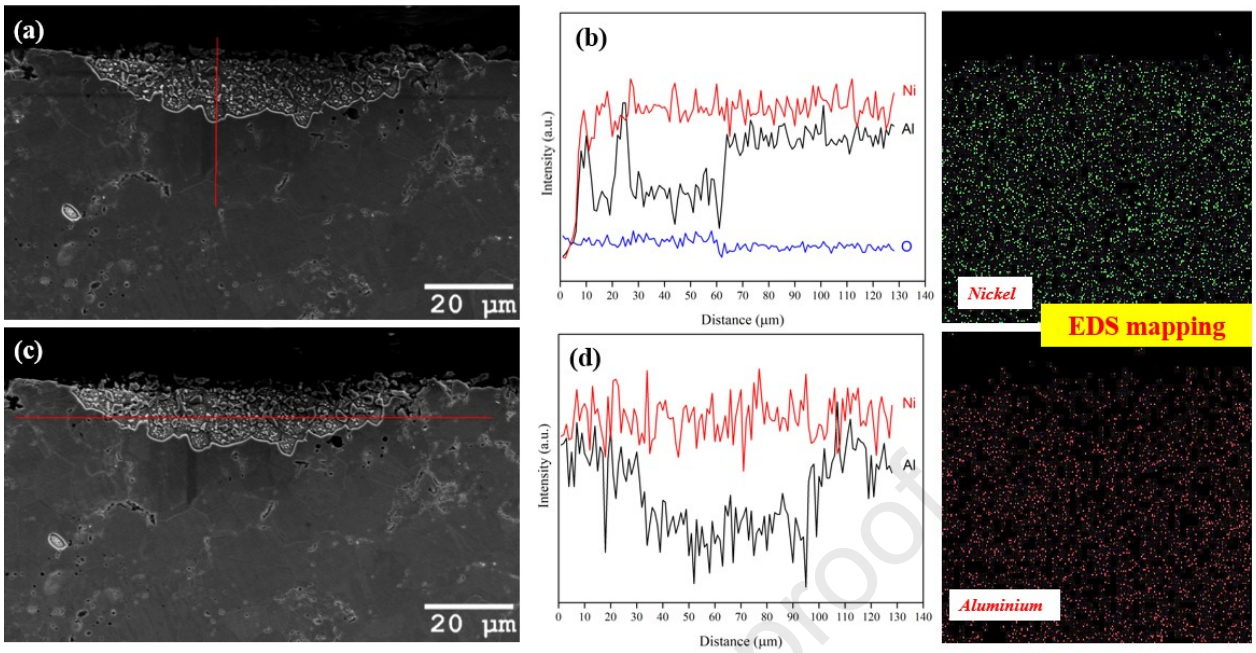

Journal Pre-proof

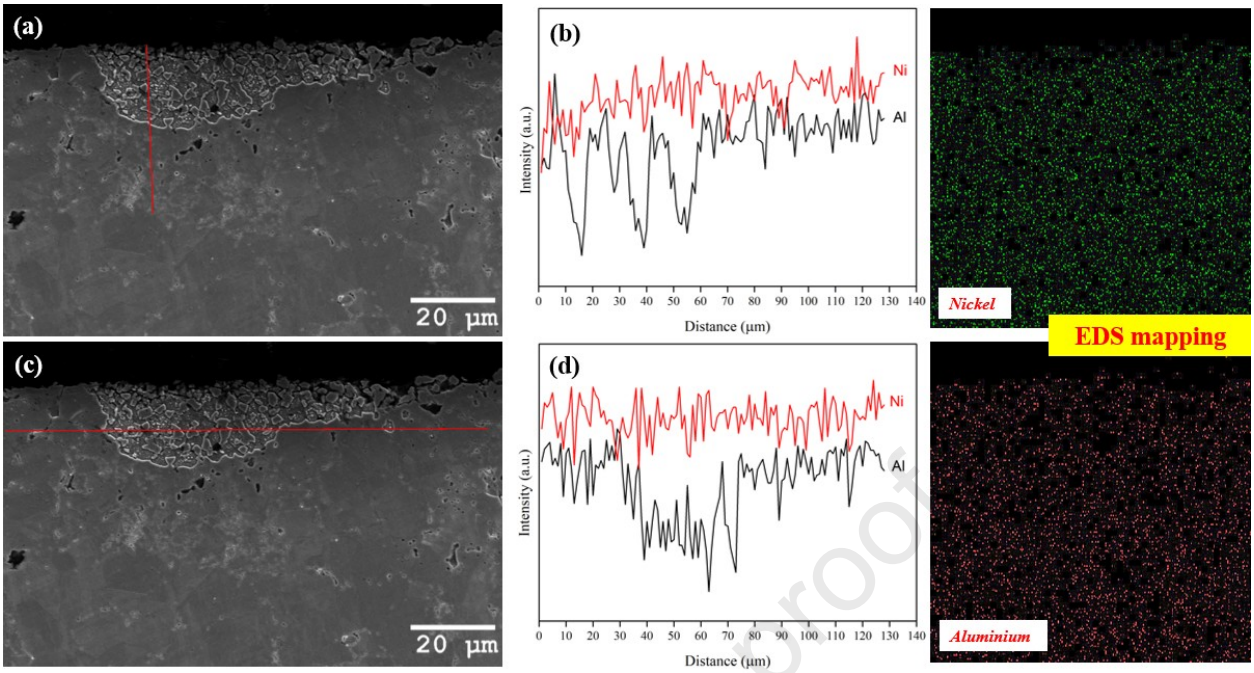

Journal Pre-proof

Highlights

- Solidification in Ni-Al alloy depending on variable aluminum content is modeled with CALPHAD approach.
- High density 85Ni:15Al wt.% powder metallurgical alloy is successfully produced using SPS.
- By using variable laser parameters, remelting zones are formed on the surface of the alloy and surface/subsurface metallurgical features are investigated.
- The scratch behavior of remelted regions under varying loads is characterized.
- The formation of the eutectic Ni_3Al-NiAl phase on remelting provides significant resistance to scratching.

Journal Pre-proof

Journal Pre-proof

Declaration of Interest Statement

☒ The authors declare that they have no known competing financial interests or personal relationships that could have appeared to influence the work reported in this paper.

☐ The authors declare the following financial interests/personal relationships which may be considered as potential competing interests:

Journal Pre-proof